

# Structural and Optical Properties of PbS Thin Films Deposited by Pulsed Laser Deposited (PLD) Technique at Different Annealing Temperature

Kadhim A. Aadim<sup>1</sup>, Abdul-Majeed E. Ibrahim<sup>2</sup>, Jassim M. Marie<sup>2,\*</sup>

<sup>1</sup>Department of Physics, University of Baghdad, College of Sciences

<sup>2</sup>Department of Physics, University of Tikrit, College Of Education

\*Corresponding author: jaassim74@gmail.com

**Abstract** Lead sulphide (PbS) thin films has attracted interest due to its potential applications in optoelectronics devices, gas sensors, solar cell technology and transparent conducting electrodes. Thin films were grown on glass substrates by pulsed laser deposition (PLD) technique at room temperature and different annealing temperatures (573, 673 and 773) K. The structural measurements for PbS thin film show face-centered-cubic structure. Atomic force microscopy (AFM) was used to examine PbS surface. The films exhibit more homogeneity. The root mean square (r.m.s), surface roughness and average grain size were increased After annealing. The optical properties of PbS thin films are studied as a function to wavelength in region (375 - 1100) nm. The optical transmittance of PbS thin films shown that the transparency decreases with increase of annealing temperature. The direct energy gap for PbS thin film was decreases with increasing of annealing temperature for all sample due to the growth of the crystallites. The optical constants such as refractive index, extinction coefficient and dielectric constant were also calculated.

**Keywords:** annealing temperature, optical properties of PbS, (PLD) technique

**Cite This Article:** Kadhim A. Aadim, Abdul-Majeed E. Ibrahim, and Jassim M. Marie, "Structural and Optical Properties of PbS Thin Films Deposited by Pulsed Laser Deposited (PLD) Technique at Different Annealing Temperature." *International Journal of Physics*, vol. 5, no. 1 (2017): 1-8. doi: 10.12691/ijp-5-1-1.

## 1. Introduction

Lead sulphide (PbS) is an important direct narrow gap semiconductor material with an approximate energy gap of 0.4 eV at 300K and a relatively large excitation Bohr radius of 18nm [1]. Class of semiconductor materials is now occupying an outstanding situation in the basic research and solid state technology. In this category, PbS is a IV-VI compound semiconductor has a cubic lattice with unit cell face center cubic. These properties make PbS very suitable for infrared detection application [2]. This material has also been used in many fields such as photography, Pb<sup>2+</sup> ions selective sensors and solar absorption [3,4].

In addition, PbS has been utilized as photoresistance, diode lasers, humidity and temperature sensors, decorative and solar control coatings [5]. These properties have been correlated with the growth conditions and the nature of substrates. For these reasons, many research groups have shown a great interest in the development and study of this material by various deposition processes such as electrodeposition, spray pyrolysis, photoaccelerated chemical deposition microwave-heating, chemical bath deposition (CBD) [6], and PLD. Furthermore, PLD is more flexible than other conventional techniques, and, it is feasible to control the thickness of films. In the current

work, we report the structural and optical properties of PbS thin films on glass substrate grown by PLD method at various substrate temperature [7].

## 2. Experimental Work

PbS thin films are prepared by PLD technique. The experiment was carried inside a vacuum chamber at vacuum ( $10^{-3}$  Torr) conditions. PbS by BDH chemical Ltd (England) with purity (98%) of these materials were mixed in gate mortar was used to form the target as a disk of 1.5cm diameter and 0.3cm thickness using hydraulic piston type (SPECAC) under pressure of 6 tons for 10 minute. It should be as dense and homogenous as possible to ensure a good quality of the deposit. The nature of the substrate is extremely important because it greatly influences the properties of the films deposited on it. The effectiveness of cleaning of substrates has a strong effect on the adhesion properties of the deposited films. In this work glass slides which were used to study the structural, surface morphology, optical properties of PbS films. The set-up of laser which shows the arrangement of the substrate holders and target inside the chamber with respect to the laser beam. Nd: YAG laser (Huafei Tongda Technology- DIAMOND-288 pattern EPLS) Power= 500 m J, F = 6 HZ,  $\lambda = 1064$  nm Number of shots = 500 pulse. The focused Nd: YAG SHG Q-switching laser incident beam

coming through a window is making an angle of  $45^\circ$  with the target surface.

## 2.1. Structure and Composition Measurements

### 2.1.1. X-Ray Diffraction

The structure of PbS thin films grown on glass substrates by PLD method at room temperature and different annealing temperatures, were studied by X-ray diffraction (XRD) techniques using a (Philips PW) X-ray diffractometer system. This system recorded the intensity as a function of Bragg's angle.

The grain size ( $D$ ) of the crystalline material which, plays the important role in the material properties can be estimated easily from the X-ray spectrum by means of full width at half-maximum (FWHM) method that is often calculated by Scherrer formula;

$$D = \frac{0.94\lambda}{\beta \cos \theta} \quad (1)$$

Where  $K= 0.9$ ,  $\lambda$  is the wave length of incident X- ray radiation,  $\beta$  is the intrinsic full width at Half Maximum of the Peak, and  $\theta$  is the Bragg's diffraction angle of the respective XRD Peak.

### 2.1.2. Atomic Force Microscope (AFM)

The film surface topography of the synthesized was studied To examine the grain size and root mean square of

roughness of PbS thin film, an atomic force microscope (AFM) was used. All the samples were studied by taking image for the films surface with tapping mode using atomic force microscope (AA3000 Scanning Probe Microscope SPM. Angstrom Ad-Vance Inc, tip NSC35/AIBS).

### 2.1.3. Optical Properties Measurements

The optical properties of films on glass Substrat with deposited at room temperature and different annealing temperature at (573, 673 and 773) K have been measured. The optical measurements of thin films depend on, thickness, homogeneity, structure, materials used and the preparation conditions were measured using UV/ Visible SP-8001 spectrophotometer over the range (375-1100) nm. This spectrometer contains two light sources Deuterium and Tungsten lamp within the wavelengths range 190–390 nm and 390–1100 nm of the spectrum respectively. The output data of wavelength, transmittance and absorbance are used in a computer program to deduce the optical energy band gap ( $E_g$ ) fundamental optical edge and all optical constants. The optical band gab was estimated graphically by applying the Tauc model, the band gap of the deposited material with sharp fall off can be deduced from a plot of the squared absorption coefficient  $(\alpha h\nu)^2$  versus photon energy ( $h\nu$ ) by extrapolating the straight line of the plot to intersect the energy axis. By measuring the absorbance and transmittance spectra one can measure the absorption coefficient( $\alpha$ ), the forbidden energy gap, refractive index( $n$ ), extinction coefficient( $k$ ), and dielectric constants (the real  $\epsilon_r$  and imaginary  $\epsilon_i$ ) were calculated for these films.

Table 1. Effect of annealing temperature on the structural properties of PbS thin films

Ta (K)	2 $\theta$ (Deg.)	FWHM (Deg.)	$d_{hkl}$ Exp.(Å)	G.S (nm)	$d_{hkl}$ Std.(Å)	hkl	Phase	card No.
	31.1037	0.4013	2.8731	20.6	2.8582	(111)	Pb	96-900-8478
<b>RT</b>	35.9866	0.6689	2.4936	12.5	2.4753	(200)	Pb	96-900-8478
	52.1070	0.6020	1.7538	14.7	1.7503	(202)	Pb	96-900-8478
	62.0067	0.5351	1.4955	17.3	1.4926	(311)	Pb	96-900-8478
	65.0836	0.5351	1.4320	17.6	1.4291	(222)	Pb	96-900-8478
	25.9532	0.2676	3.4304	30.5	3.4246	(111)	PbS	96-901-3404
<b>573</b>	29.9666	0.6020	2.9795	13.7	2.9657	(200)	PbS	96-901-3404
	43.0100	0.8695	2.1013	9.8	2.0971	(202)	PbS	96-901-3404
	50.9699	0.6020	1.7903	14.6	1.7884	(311)	PbS	96-901-3404
	53.3110	0.6689	1.7170	13.3	1.7123	(222)	PbS	96-901-3404
	25.9532	0.2676	3.4304	30.5	3.4246	(111)	PbS	96-901-3404
<b>673</b>	30.0334	0.4682	2.9730	17.6	2.9657	(200)	PbS	96-901-3404
	42.8763	0.5351	2.1075	16.0	2.0971	(202)	PbS	96-901-3404
	51.0368	0.5351	1.7881	16.5	1.7884	(311)	PbS	96-901-3404
	53.4448	0.4683	1.7130	19.0	1.7123	(222)	PbS	96-901-3404
	25.9511	0.2610	3.4306	31.3	3.4246	(111)	PbS	96-901-3404
<b>773</b>	30.1003	0.2675	2.9665	30.8	2.9657	(200)	PbS	96-901-3404
	42.8700	0.4013	2.1078	21.3	2.0971	(202)	PbS	96-901-3404
	51.0355	0.3345	1.7881	26.3	1.7884	(311)	PbS	96-901-3404
	53.5086	0.4014	1.7111	22.2	1.7123	(222)	PbS	96-901-3404

### 3. Results and Discussion

#### 3.1. Structural Properties

PbS thin film were deposited on glass substrates prepared by PLD. XRD give the confirmation of presence of Pb in the prepared film as shown in Figure 1. It is seen that Pb exists at room temperature which are distinct peaks in (31.10°, 35.98° and 52.10°) values respectively. The films were fabricated at the lowest temperature have the least crystalline quality as was observed in XRD patterns, but at the higher temperature gained better crystallinity. Figure 1 shows the typical XRD pattern of the PbS thin film samples for different annealing temperatures (573,673,and 773) K. It shows several five diffraction peaks at  $2\theta$  values of (25.95°, 29.96°, 43.01°, 51.03° and 53.31°). These were assigned to the diffraction lines produced by (111), (200), (220), (311) and (222) planes of the face-centered-cubic structure of PbS confirmed by standard ASTM data. XRD patterns of all the PbS thin films showed sharp (111) and (200) peaks along with minor peaks of (220), (311), and (222) planes corresponding of the deposited PbS films were calculated

and the results were reported in Table 1. For all the films the preferential orientation value of (111) plane has the highest value compared to that of the other planes indicating a strong orientation growth along that plane. This result on preferential orientation is strongly supported with earlier report Mohammad and Rajashree [8,9]. The variation in preferential orientation factor  $d_{hkl}$  for (111) as a function of annealing temperature shown in Figure 1, predicts that (111) is maximum for the film coated at (773)K, indicating better crystallinity. These XRD results confirm the proper phase formation of the PbS films. The crystallographic structure of the prepared PbS thin films was determined using a high resolution X-ray diffractometer. No other peaks are detected in the XRD pattern, confirming high purity of the PbS thin films. The intensity of the peaks increases with increase in annealing temperature which reveals that crystallinity of the film improves with increase in annealing temperature. The crystalline grain size (D) of the PbS films was determined with the Scherrer formula. This effect can be related to the increase of grain size with increasing annealing temperature this result was in agreement with Jana and Laxmi [10,11].

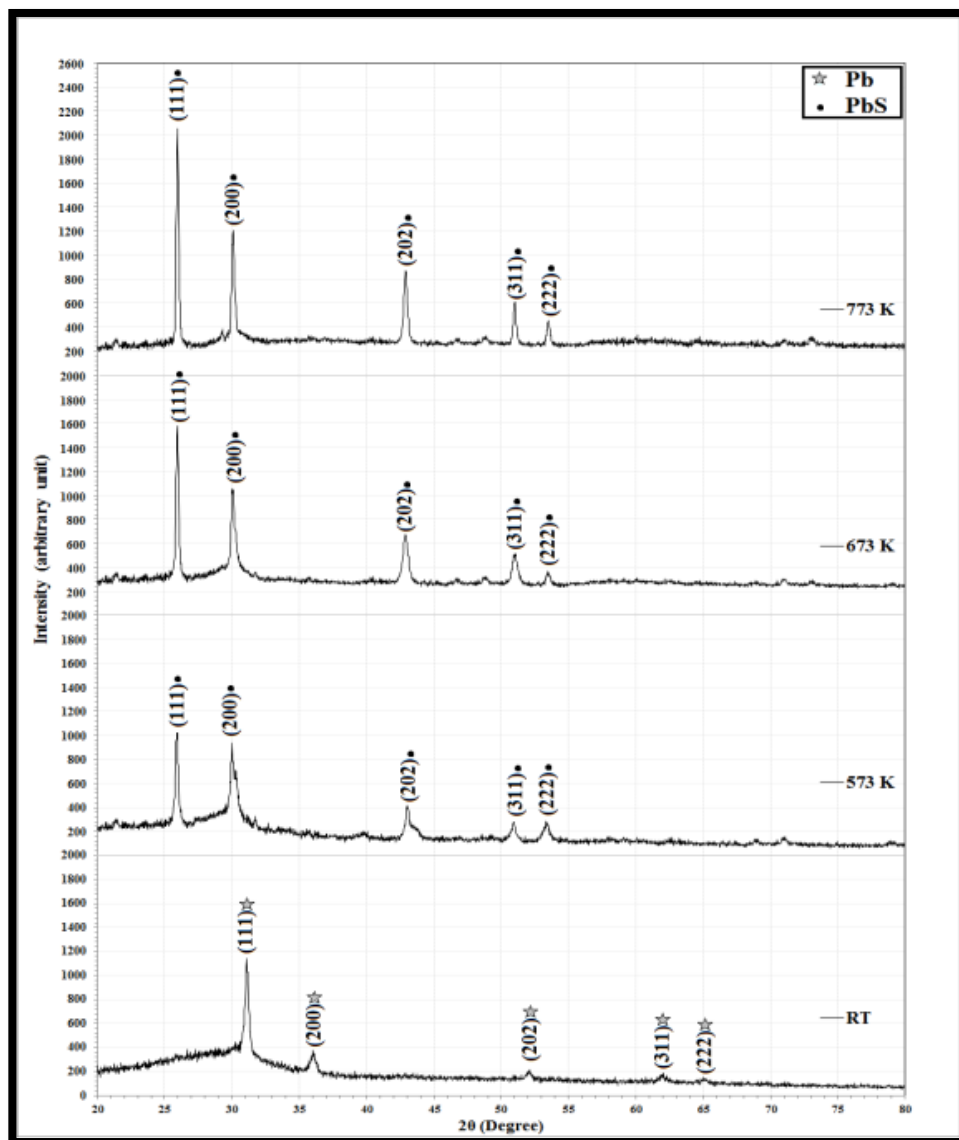


Figure 1. The XRD of PbS thin films at different annealing temperatures (RT, 573, 673, and 773) K

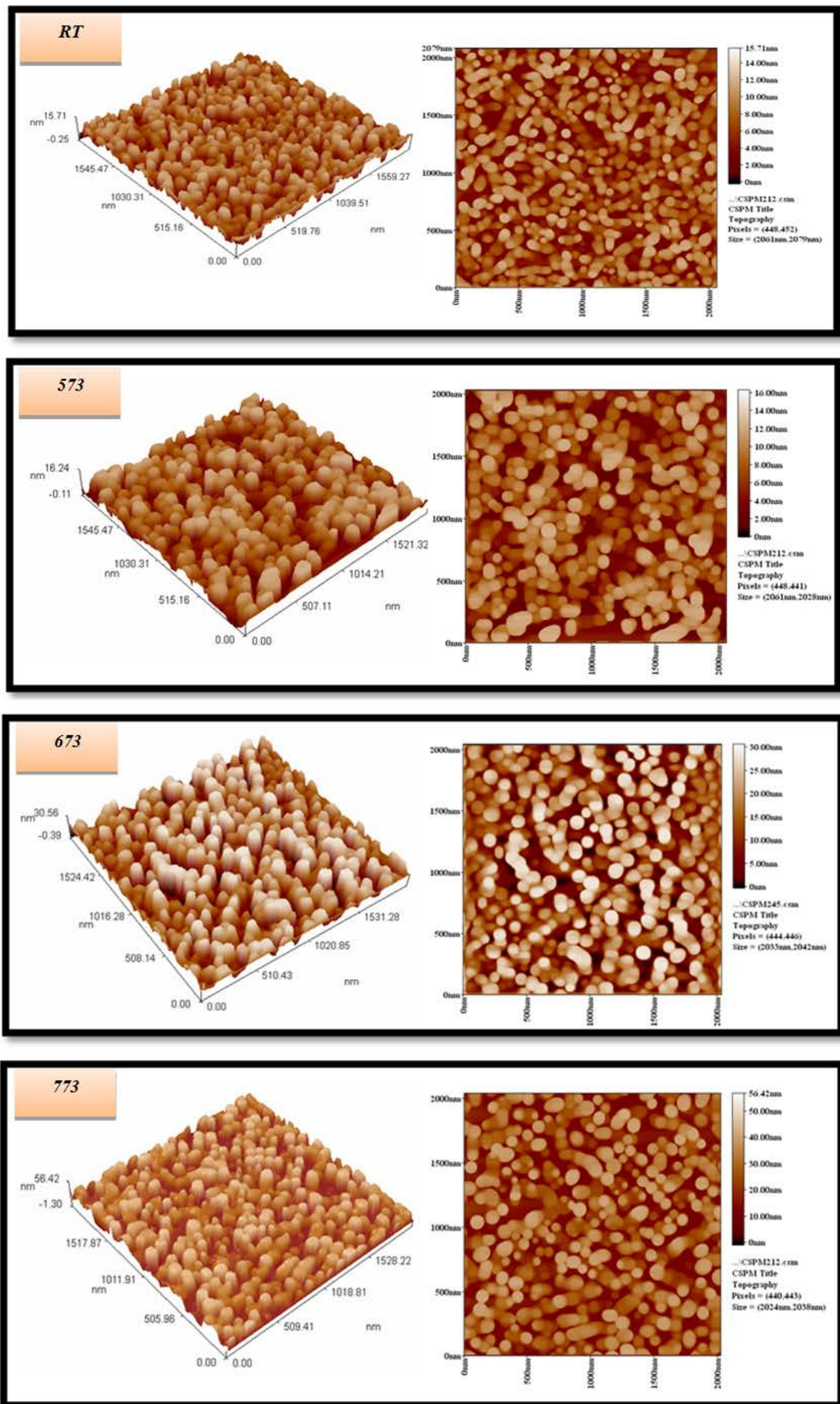


Figure 2. 2D and 3D AFM images pure PbS thin films

**Table 2. Morphology Parameters for PbS thin films**

Sample	Ta (K)	Average diameter (nm)	Average roughness (nm)	Peak –Peak (nm)	r.m.s (nm)
PbS	RT	77.08	2.34	12.2	2.71
	573	96.12	2.62	11	3.07
	673	97.16	6.77	28.7	7.9
	773	110.44	8.34	31.3	9.53

### 3.1.2. Atomic Force Microscope (AFM) Analysis

AFM studies reveal that there is a dramatic change in the morphologies of the deposited PbS thin films on glass substrates at different annealing temperatures (573, 673, and 773) K. AFM images of the surface morphology recorded on samples of the PbS thin films deposited are shown in Figure 2. AFM parameters contain average diameter, average roughness, average root mean square (r.m.s) roughness and peak –peak value of experiments and the data of results observed in these experiments were collected for these samples have been shown in Table 2. A dense surface of the thin films was obtained at all cases. The thin films were composed of multilayered grains. AFM images showed the grain diameter of PbS as function of different annealing temperature, it is appears that the particle size increased with increasing of the annealing temperature. The same relation between the average roughness, average (r.m.s) roughness and peak -peak value and the annealing temperature has been observed. In addition, preferential film growth improved with increasing annealing temperature which was in accordance with XRD analysis.

## 3.2. Optical Properties

In this work we study the influence of the annealing temperature on the optical properties of PbS thin films at deposited on glass substrates by PLD. The first part will be devoted to the study the transmittance. The second will proceed in energy gap of PbS thin films. The third part will proceed in determine the refractive index, the extinction coefficient, dielectric constant, and optical constant measurements at near normal incidence were performed over a spectral ranging between (375- 1100)nm on PbS thin films deposited on glass substrate at room temperature and different annealing temperatures.

### 3.2.1. The Transmission Spectrum (T)

The transmission of PbS thin films which deposited on glass substrates were determined optical spectra for a series of films were carried out with a UV-VIS-NIR spectrophotometer in the range of (375–1100)nm prepared at room temperature and different annealing temperatures (573, 673, and 773) K by PLD is over 60 %. Figure 3 show that the transparency decreases with increase of annealing temperature because of the increasing thickness with temperature and the transmittance increase with increasing wavelength but is low for wavelength smaller than (600) nm. This result is comparable to one which reported by researchers Yasmeen and Jana [7,10]. As it is clear from spectra, the films have a steep optical absorption feature, indicating good homogeneity in the shape and size of the nanocrystalline and low defect density near the band edge. This is in agreement with the results obtained by Srinivasan [12].

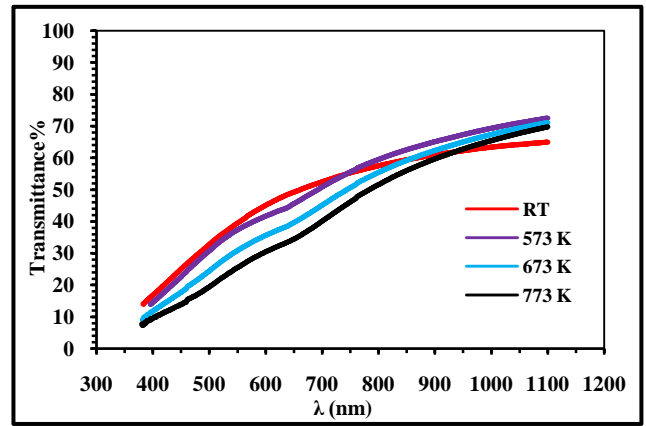


**Figure 3.** The Variation of the Transmittance with Wavelength of the PbS Films with Different Annealing Temperatures.

### 3.2.2. Optical Energy Gap ( $E_g$ )

Energy gap ( $E_g$ ) is the separation between valance and conduction bands of semiconductor. Variation of  $(\alpha h\nu)^2$  as a function of photon energy ( $h\nu$ ) is plotted in the Figure 4. As observable,  $(\alpha h\nu)^2$  varies linearly with  $(h\nu)$  after a certain amount of photon energy, confirming the direct nature transition mode in the PbS films. The  $E_g$  can be obtained by extrapolating the straight-line portion of graph to zero absorption coefficient with deposition at different annealing temperatures (573, 673, and 773) K. It is observed from the Table 3 the  $E_g$  values of PbS films decreases with increase annealing temperature which lies in the red region of the visible spectrum due to agglomeration of the Nano-crystallites into larger crystallites. This is an agreement with the results obtained by Rajashree and Thangavel [9,13].

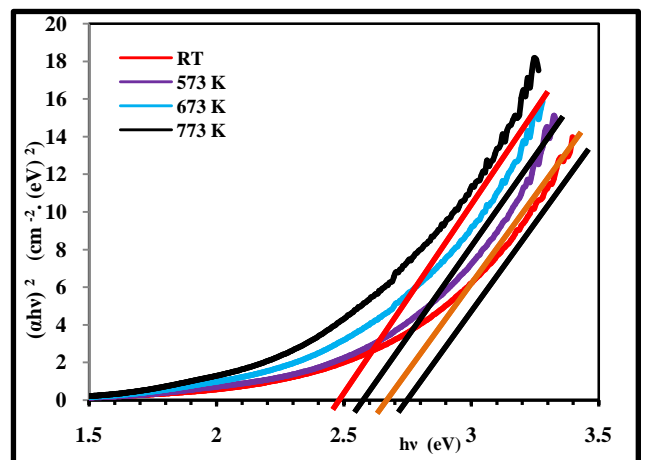


**Figure 4.**  $(\alpha h\nu)^2$  as a function of  $h\nu$  for of the PbS Films with Different Annealing Temperatures

**Table 3. Optical Energy gap with Different Annealing Temperatures**

Ta K	RT	573	673	773
$E_g$ (eV)	2.71	2.63	2.52	2.45

These values are greater than the bulk material [19]. It may be due to the fact that the amorphous or nanocrystalline films show energy gap higher than of the corresponding bulk materials. The increase in the  $E_g$  is due the Nano-crystalline nature of the PbS thin film. This is in agreement with the results obtained by Hussain, ALI and Uhuegbu [14,15,16].

### 3.2.3. Absorption Coefficient ( $\alpha$ )

The fundamental absorption edge of the PbS films, which corresponds to electron excitation from the valance band to conduction band, can be used to determine the nature and value of the optical energy gap, the absorption coefficient  $\alpha$  was determined from the region of high absorption. Figure 5 show the optical absorption coefficient as a function of incident wave length on PbS films at room temperatures and different annealing temperatures (573, 673, and 773) K. It is noticed from these figures that  $\alpha$  increases with increasing of annealing due to the decreasing of energy gap. We can evidently see that thin film In the shorter wavelength the absorption coefficient exhibits high values of ( $\alpha > 10^4 \text{ cm}^{-1}$ ) which causes the increase of the probability of the occurrence direct transitions and then  $\alpha$  decreases with increasing of wavelength. The values of the absorption coefficient are nearly in agreement with values reported by Yasmeen and Srinivasan [7,12].

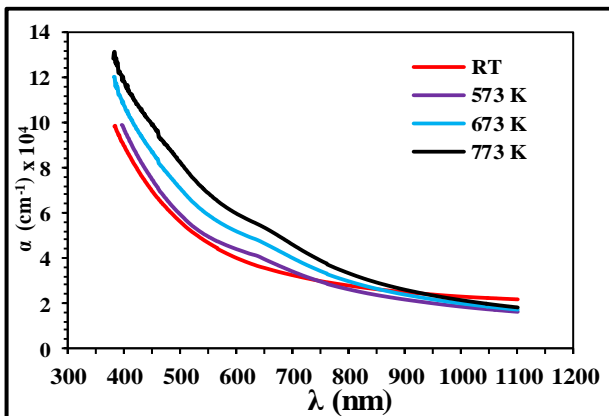


Figure 5. The Absorption Coefficient  $\alpha$  for PbS Films with Different Annealing Temperatures

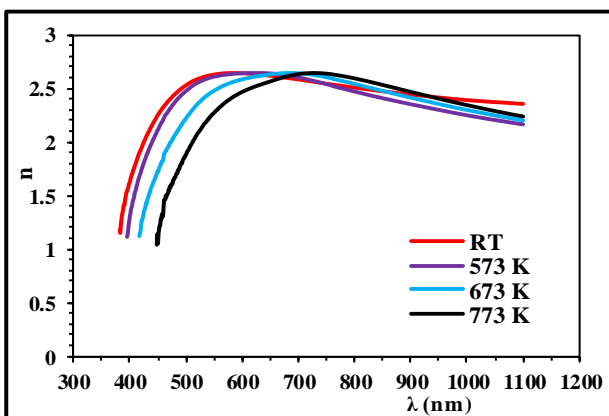


Figure 6. The Variation of The Refractive Index ( $n$ ) With Wavelength of PbS Films with Different Annealing Temperatures

### 3.2.4. Refractive Index ( $n$ )

The refractive index is the ratio between speed of light in vacuum to its speed in material which doesn't absorb this light. The variation of the refractive index versus wavelength in the range (375-1100) nm at room temperature and different annealing temperatures have been depending on the reflectance values is shown in Figure 6. The maximum value of  $n$  for all films is approximately equal the value of (2.6) and we can notice from these figures that the refractive index in general decreases slightly with increasing of annealing temperatures. It is clear from the graph  $n$  value decreasing with increasing ( $\lambda$ ) after maximum peak with a different manner. The explanation of this behavior may be related to the polarization of thin film because  $n$  depends on material polarization where with increasing polarization the velocity of light was decreased so  $n$  changed. The polarization depends on crystallinity and on grain size of thin film so these depend on preparation conditions. This is in agreement with Vinodkumar and El-Desoky [17,18].

### 3.2.5. Extinction Coefficient ( $k$ )

The behavior of the extinction coefficient ( $k$ ) is nearly similar to the corresponding absorption coefficient. Figure 7 shows the extinction coefficient as a function of wavelength for PbS films at room temperature and different annealing temperature. We can observe from the Figure 7 and Table 4 that the extinction coefficient, in general, increasing with increasing of annealing temperature for all films. This is attributed to the same reason mentioned previously, decreases the optical energy gap as a result of absorbance increment. This result agrees well with literature Abbas [19].

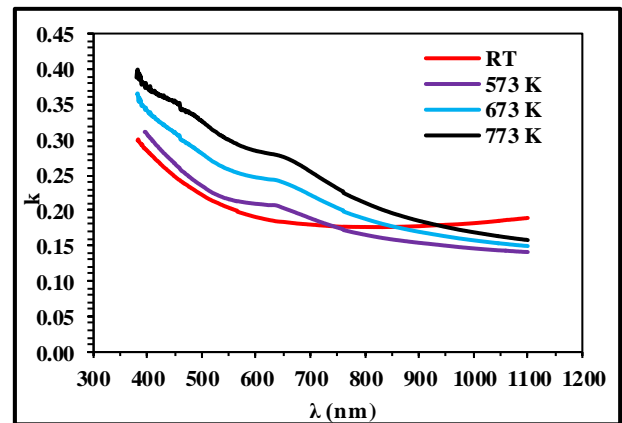
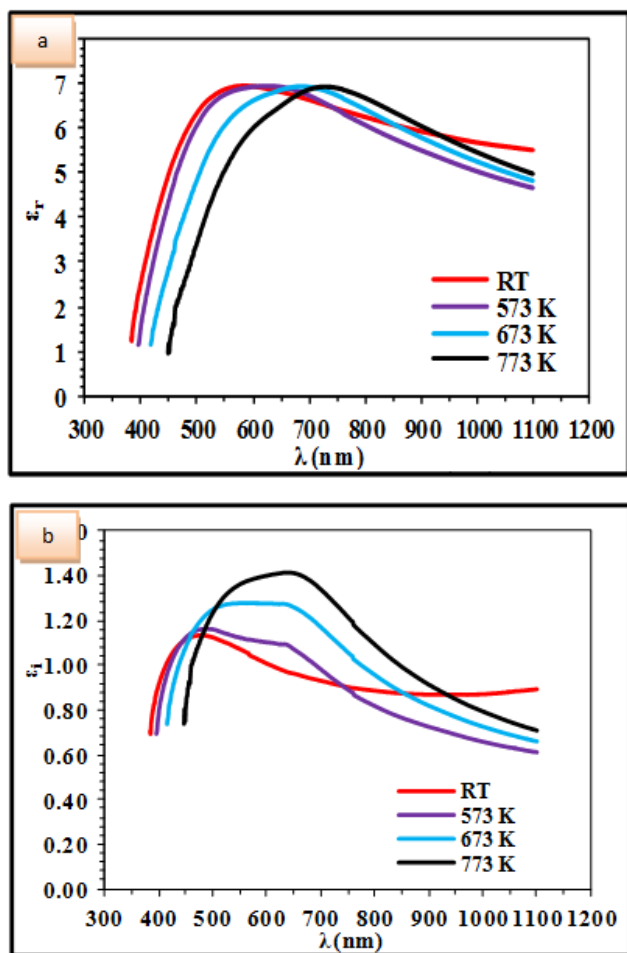


Figure 7. The Variation of The Extinction Coefficient With Wavelength of PbS Films with Different Annealing Temperatures

Table 4. Values of Refractive index ( $n$ ), Extinction coefficient ( $k$ ), Real ( $\epsilon_r$ ) and Imaginary ( $\epsilon_i$ ) Dielectric Constant for PbS films (at 500 nm wavelength)

Ta (K)	T%	$\alpha \text{ (cm}^{-1}\text{)}$	K	n	$\epsilon_r$	$\epsilon_i$	$E_g \text{ (eV)}$
RT	32.75	55807	0.222	2.530	6.350	1.124	2.71
573	30.73	59004	0.235	2.476	6.076	1.163	2.63
673	24.43	70470	0.281	2.221	4.855	1.246	2.52
773	19.42	81936	0.326	1.886	3.450	1.230	2.45



**Figure 8.** The Variation of The Dielectric Constants a-real part ( $\epsilon_r$ ) and b- imaginary ( $\epsilon_i$ ) parts With Wavelength of PbS Films with Different Annealing Temperature

### 3.2.6 Dielectric Constant

Real and imaginary part of dielectric constant values versus wavelength in the range of (375–1100) nm for PbS thin film with different annealing temperatures. The plots of real and imaginary part of all samples were illustrated in Figure 8(a,b). Figure 8(a) show that all samples behave like the refractive index samples because of the smaller value of ( $k^2$ ) compared with ( $n^2$ ), Figure 8(b) shows that all samples behave like the extinction coefficient samples which means that the real and imaginary part increased with increasing of annealing temperatures. It is seen that the real part of dielectric constant decreased by increasing wavelength and the values of real part is higher than imaginary part as shown in Table 4. These measurements are agreed with the data of M.Abbas [20].

## 4. Conclusions

PbS Thin film were deposited on glass substrates are prepared by means of simple and low cost by PLD technique. Post-annealing process helps to improve the crystalline quality thin films. The effect of growth temperature on structural and optical properties was studied. The typical XRD pattern of the PbS samples for different annealing temperatures show planes of the face-centered-cubic structure. The transmission of PbS

thin films which deposited on glass substrates were determined is over 60 %.The band gap energy values of thin films decreases with increase annealing temperature which lies in the red region of the visible spectrum due to agglomeration of the Nano-crystallites into larger crystallites.

## References

- [1] Sudad S. Ahmed, Eman K. Hassan & Fatn Emad, "PbS nano thin film photoconductor", International Journal of Physics and Research (IJPR) ISSN 2250 -0030 Vol. 3, Issue 3, 21-26, (2013).
- [2] S. Seghaier, N. Kamouna, R. Brini, A.B. Amarac, "Structural and optical properties of PbS thin films deposited by chemical bath deposition", materials Chemistry and Physics, 97, 71-80, (2006).
- [3] Uhuegbu, Chidi C, "Growth and Characterization of Lead Sulphide Thin Film for Solar Cell Fabrication", Canadian Journal on Scientific and industrial research vol.2 No. 6, 230, (2011).
- [4] Mosiori, Cliff Orori, Njoroge, Walter N., Okumu, John, "Optical and Electrical Properties of Pbs Properties of Pbs Thin Films Grown by Chemically Bath Deposition [CBD] at Different Lead Concentrations", International Journal of Advanced Research in Physical (IJARPS) Volume 1, Issue (IJARPS) Volume 1, Issue Science(IJARPS) Volume1, issue, pp 25-32, (2014).
- [5] Amusan, J., Fajinmi, G. and Sasusi, Y., "Deposition time dependence on absorptivity of chemically deposited lead sulphide thin films", Research Journal of Applied Sciences, 9: 931-937, (2007).
- [6] S. Seghaier, N. Kamoun, R. Brini, A.B. Amara. "Structural and optical properties of PbS thin films deposited by chemical bath deposition" Materials Chemistry and Physics, 97, 71-80, (2006).
- [7] Dr. Yasmeen Z. Dawood, Suad M. Kadhim, Ayad Z. Mohammed. "Structure and Optical Properties of Nano PbS Thin Film Deposited by Pulse Laser Deposition", vol.32,no.9,pp.1723- 1730, (2015)
- [8] Mohammad G. Faraj and Halo D. Omar" The Effect of Substrate Temperature on the Structural Properties of Spray Pyrolysed Lead Sulphide (PbS) Thin Films" Volume II, Article ID: ARO.10044, 4 pages, No 2, (2014).
- [9] C.Rajashree, A.R. Balu, V.S.Nagarethinam. "Substrate Temperature effect on the Physical properties of Spray deposited Lead sulfide Thin Films suitable for Solar control coatings" Vol.6, No.1, pp 347-360, (2014).
- [10] S. Jana, R. Thapa, R. Maity a, K.K. Chattopadhyay" Optical and dielectric properties of PVA capped nanocrystalline PbS thin films synthesized by chemical bath deposition" Physica E 40 3121-3126, (2008).
- [11] Laxmi J. Tomar, Piyush J. Bhatt, Rahul K. Desai, Bishwajit S. Chakrabarty. " Synthesis and Characterization of Nanostructured PbS Thin film" University of Baroda, Vadodara, India. (2014).
- [12] P. Srinivasan and P. Rajesh. "Effect of temperature on the structural and optical properties of chemically deposited PbS thin films" Elixir Thin Film Tech. 42, 6206-6208, (2012).
- [13] S. Thangavel, S. Ganesan, K. Saravanan. "Annealing effect on cadmium in situ doping of chemical bath deposited PbS thin films". Thin Solid Films 520 5206-5210, (2012).
- [14] A. Hussain, A Begum and A Rahman. "Electrical and optical properties of nanocrystalline lead sulphide thin films prepared by chemical bath deposition" Indian J Phys 86(8): 697-701, (2012)
- [15] ALI M. MOUS, SELMA M. H. AL-JAWAD & SUAD M. KADHIM AL-SHAMMARI" PERFORMANCE OF A NANOSTRUCTURED PbS/Si HETROJUNCTION DETECTOR BY CBD". Vol. 3, Issue 4, 11-18, (2013).
- [16] Uhuegbu, Chidi C. "Growth and Characterization of Lead Sulphide Thin Film for Solar Cell Fabrication". Canadian Journal on Scientific and Industrial Research Vol. 2 No. 6, June (2011).
- [17] R. Vinodkumar, I. Navas, K. Porsezian, V. Ganesan, N.V. Unnikrishnan, V.P. Mahadevan Pillai, "Structural, spectroscopic and electrical studies of nanostructured porous ZnO thin films prepared by pulsed laser deposition". Spectrochim. Acta A 118, 724, (2014).
- [18] M. M. El-Desoky • M. A. Ali • G. Afifi H. Imam. "Annealing effects on the structural and optical properties of growth ZnO thin films fabricated by pulsed laser deposition (PLD)". (2014).

- [19] M. Abass, E..Al-Fawadi and A-K. Al-Samuraee, "Preparation of Nanocrystalline PbS Thin Films by Chemical Bath Deposition". *Joining of Advanced and Specialty Materials*, (2009).
- [20] M.M.Abbas, A. Ab-M. Shehab, A-K. Al-Samuraee, and N-A. Hassan. "Effect of Deposition Time on the Optical Characteristics of Chemically Deposited Nanostructure PbS Thin Films". *Energy Procedia* 6, 241-250, (2008).

# Structural-Parametric Model Electromagnetoelastic Actuator Nanodisplacement for Mechatronics

Sergey Mikhailovich Afonin \*

Department of Intellectual Technical Systems, National Research University of Electronic Technology (MIET), Moscow, Russia  
\*Corresponding author: [eduems@mail.ru](mailto:eduems@mail.ru)

**Abstract** Electromagnetoelastic actuator have been used successfully to nanodisplacement for mechatronics systems in nanotechnology, electronic engineering, microelectronics, nanobiology, power engineering, astronomy. Linear structural-parametric model, parametric structural schematic diagram, transfer functions of the simple electromagnetoelastic actuator nanodisplacement for the mechatronics systems are obtained. For calculation of the mechatronics system with piezoactuator the parametric structural schematic diagram and the transfer functions of the piezoactuator are obtained. A generalized parametric structural schematic diagram and transfer functions of the piezoactuator are constructed. This work describes the linear structural-parametric model of the simple piezoactuator for the mechatronic in the static and dynamic operation modes in contrast solving its electrical equivalent circuit.

**Keywords:** *electromagnetoelastic actuators, structural-parametric model, piezoactuator, deformation, nanodisplacement, transfer functions*

**Cite This Article:** Sergey Mikhailovich Afonin, "Structural-Parametric Model Electromagnetoelastic Actuator Nanodisplacement for Mechatronics." *International Journal of Physics*, vol. 5, no. 1 (2017): 9-15. doi: 10.12691/ijp-5-1-2.

## 1. Introduction

For mechatronics, nanotechnology, electronic engineering, microelectronics, nanobiology, power engineering, astronomy, antennas satellite telescopes and adaptive optics are promising the electromechanical actuators based on electromagnetoelasticity (piezoelectric, piezomagnetic, electrostriction, and magnetostriction effects). Piezoactuator - piezomechanical device intended for actuation of mechanisms, systems or management based on the piezoelectric effect, converts electrical signals into mechanical movement or force. Piezoactuators are used in the majority of scanning tunneling microscopes (STMs), atomic force microscopes (AFMs), in the adaptive optics of big telescopes, for example, European Extremely Large Telescope (E-ELT) and Large Synoptic Survey Telescope (LSST) [1-25].

In the present paper is solving the problem of building the linear structural-parametric model of the simple electromagnetoelastic actuator nanodisplacement the mechatronics systems for static and dynamic operation modes in contrast solving its electrical equivalent circuit Cady-Mason. Equivalent circuits of the piezoelectric transducers are designed for calculation of piezoelectric transmitters and receivers [9,10,11,12]. For the next new paper about the control system of the piezoactuator will be used, for example, the nonlinear hysteresis model for correction control system of the piezoactuator [8].

By solving the wave equation with allowance methods of mathematical physics for equation electromagnetoelasticity, the boundary conditions on loaded working surfaces of

actuators, the strains along the coordinate axes, it is possible to construct the linear structural-parametric model of the actuator for the mechatronics systems [14-23].

## 2. The Structural-Parametric Model of the Electromagnetoelastic Actuator for Mechatronics Systems

For the piezoactuator its deformation corresponds to stressed state. If the mechanical stress  $T$  is created in the piezoelectric element, the deformation  $S$  is formed in it.

There are six stress components  $T_1, T_2, T_3, T_4, T_5, T_6$ , the components  $T_1 - T_3$  are related to extension-compression stresses,  $T_4 - T_6$  to shear stresses.

The matrix state equations [12] connecting the electric and elastic variables for polarized ceramics for the mechatronics systems have the form

$$\mathbf{D} = \mathbf{d}\mathbf{T} + \boldsymbol{\varepsilon}^T \mathbf{E}, \quad (1)$$

$$\mathbf{S} = \mathbf{s}^E \mathbf{T} + \mathbf{d}^t \mathbf{E}, \quad (2)$$

where the first equation describes the direct piezoelectric effect, and the second - the inverse piezoelectric effect;  $\mathbf{D}$  is the column matrix of electric induction along the coordinate axes;  $\mathbf{S}$  is the column matrix of relative deformations;  $\mathbf{T}$  is the column matrix of mechanical stresses;  $\mathbf{E}$  is the column matrix of electric field strength along the coordinate axes;  $\mathbf{s}^E$  is the elastic compliance matrix for  $E = \text{const}$ ;  $\boldsymbol{\varepsilon}^T$  is the matrix of the dielectric

permeabilities for  $T = \text{const}$ ;  $\mathbf{d}^t$  is the transposed matrix of the piezoelectric modules. In polarized ceramics PZT there are five independent components  $s_{11}^E, s_{12}^E, s_{13}^E, s_{33}^E, s_{55}^E$  in the elastic compliance matrix for polarized piezoelectric ceramics, three independent components of the piezoelectric modules  $d_{33}, d_{31}, d_{15}$  in the transposed matrix of the piezoelectric modules and three independent components of the dielectric constants  $\varepsilon_{11}^T, \varepsilon_{22}^T, \varepsilon_{33}^T$  in the matrix of dielectric constants.

The direction of the polarization axis P, i.e., the direction along which polarization was performed, is usually taken as the direction of axis 3.

The generalized electromagnetoelasticity equation of the actuator [12] for mechatronics systems has the form

$$S_i = s_{ij}^{E,H,\Theta} T_j + d_{mi}^{H,\Theta} E_m + d_{mi}^{E,\Theta} H_m + \alpha_i^{E,H} \Delta\Theta, \quad (3)$$

where  $S_i$  is the relative deformation along the axis  $i$ ,  $E$  is the electric field strength,  $H$  is the magnetic field strength,  $\Theta$  is the temperature,  $s_{ij}^{E,H,\Theta}$  is the elastic compliance for  $E = \text{const}$ ,  $H = \text{const}$ ,  $\Theta = \text{const}$ ,  $T_j$  is the mechanical stress along the axis  $j$ ,  $d_{mi}^{H,\Theta}$  is the piezomodule, i.e., the partial derivative of the relative deformation with respect to the electric field strength for constant magnetic field strength and temperature, i.e., for  $H = \text{const}$ ,  $\Theta = \text{const}$ ,  $E_m$  is the electric field strength along the axis  $m$ ,  $d_{mi}^{E,\Theta}$  is the magnetostriction coefficient,  $H_m$  is the magnetic field strength along the axis  $m$ ,  $\alpha_i^{E,H}$  is the coefficient of thermal expansion,  $\Delta\Theta$  is deviation of the temperature  $\Theta$  from the value  $\Theta = \text{const}$ ,  $i = 1, 2, \dots, 6, j = 1, 2, \dots, 6, m = 1, 2, 3$ .

Let us consider the simplest electromagnetoelastic actuators for longitudinal, transverse and shift deformations in contrast the bimorph flextensional piezoactuators [1,2,3]. Piezoactuator for the longitudinal piezoelectric effect are shown in Figure 1, where  $\delta$  is the thickness. The electrodes deposited on its faces perpendicular to axis 3, the area of face is equal to  $S_0$ . In the equation (2) of the inverse longitudinal piezoelectric effect are the following parameters:  $S_3 = \partial\xi(x,t)/\partial x$  is the relative displacement of the cross section of the piezoactuator,  $d_{33}$  is the piezomodule for the longitudinal piezoelectric effect,  $E_3(t) = U(t)/\delta$  is the electric field strength,  $U(t)$  is the voltage between the electrodes of actuator,  $\delta$  is the thickness,  $s_{33}^E$  is the elastic compliance along axis 3, and  $T_3$  is the mechanical stress along axis 3.

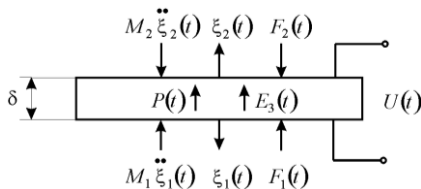


Figure 1. Piezoactuator for the longitudinal piezoelectric effect

Simultaneously solved the wave equation, the equation of the inverse longitudinal piezoeffect and the equation of forces acting on the faces of the piezoactuator. Calculations of the piezoactuators are performed using a wave equation [2,12] describing a wave propagation in a long line with damping but without distortions, in the form

$$\frac{1}{(c^E)^2} \frac{\partial^2 \xi(x,t)}{\partial t^2} + \frac{2\alpha}{c^E} \frac{\partial \xi(x,t)}{\partial t} + \alpha^2 \xi(x,t) = \frac{\partial^2 \xi(x,t)}{\partial x^2}, \quad (4)$$

where  $\xi(x,t)$  is the displacement of the section,  $x$  is the coordinate,  $t$  is time,  $c^E$  is the sound speed for  $E = \text{const}$ ,  $\alpha$  is the damping coefficient.

Using the Laplace transform, we can reduce the original problem for the partial differential hyperbolic equation of type (4) to a simpler problem for the linear ordinary differential equation [2,3,13,14].

Applying the Laplace transform to the wave equation (4) and setting the zero initial conditions, we obtain the linear ordinary second-order differential equation with the parameter  $p$

$$\frac{d^2 \Xi(x,p)}{dx^2} - \left[ \frac{1}{(c^E)^2} p^2 + \frac{2\alpha}{c^E} p + \alpha^2 \right] \Xi(x,p) = 0. \quad (5)$$

Solution of the linear ordinary second-order differential equation is the function

$$\Xi(x,p) = Ce^{-x\gamma} + Be^{x\gamma}, \quad (6)$$

where  $\Xi(x,p)$  is the Laplace transform of the displacement of the section of the actuator,  $\gamma = p/c^E + \alpha$  is the propagation coefficient. Coefficients  $C$  and  $B$  of the solution of the linear ordinary second-order differential equation are determined for the conditions

$$\begin{aligned} \Xi(0,p) &= \Xi_1(p) \text{ for } x=0, \\ \Xi(\delta,p) &= \Xi_2(p) \text{ for } x=\delta. \end{aligned} \quad (7)$$

Then, the coefficients are the following form:

$$\begin{aligned} C &= \left( \Xi_1 e^{\delta\gamma} - \Xi_2 \right) / \left[ 2\text{sh}(\delta\gamma) \right], \\ B &= \left( \Xi_1 e^{-\delta\gamma} - \Xi_2 \right) / \left[ 2\text{sh}(\delta\gamma) \right]. \end{aligned} \quad (8)$$

The solution (5) can be written as

$$\Xi(x,p) = \left\{ \begin{aligned} &\Xi_1(p) \text{sh}[(\delta-x)\gamma] \\ &+ \Xi_2(p) \text{sh}(x\gamma) \end{aligned} \right\} / \text{sh}(\delta\gamma). \quad (9)$$

The equations for the forces on the faces of the piezoactuator

$$\begin{aligned} T_3(0,p)S_0 &= F_1(p) + M_1 p^2 \Xi_1(p) \text{ for } x=0, \\ T_3(\delta,p)S_0 &= -F_2(p) + M_2 p^2 \Xi_1(p) \text{ for } x=\delta, \end{aligned} \quad (10)$$

where  $T_3(0,p)$  and  $T_3(\delta,p)$  are determined from the equation of the inverse piezoelectric effect.

For  $x=0$  and  $x=\delta$ , we obtain the following set of the equations for determining stresses in the piezoactuator [15-24]

$$\begin{aligned} T_3(0, p) &= \frac{1}{s_{33}^E} \left. \frac{d\Xi(x, p)}{dx} \right|_{x=0} - \frac{d_{33}}{s_{33}^E} E_3(p), \\ T_3(\delta, p) &= \frac{1}{s_{33}^E} \left. \frac{d\Xi(x, p)}{dx} \right|_{x=\delta} - \frac{d_{33}}{s_{33}^E} E_3(p). \end{aligned} \quad (11)$$

The set of equations (5) yield the set of equations for the linear structural-parametric model of the piezoactuator and parametric structural schematic diagram of a voltage-controlled piezoactuator for longitudinal piezoelectric effect Figure 2:

$$\begin{aligned} \Xi_1(p) &= \left[ 1 / (M_1 p^2) \right] \cdot \\ &\left\{ -F_1(p) + \left( 1 / \chi_{33}^E \right) \left[ \begin{array}{l} d_{33} E_3(p) \\ -[\gamma / \text{sh}(\delta\gamma)] \left[ \begin{array}{l} \text{ch}(\delta\gamma) \Xi_1(p) \\ -\Xi_2(p) \end{array} \right] \end{array} \right] \right\}, \quad (12) \\ \Xi_2(p) &= \left[ 1 / (M_2 p^2) \right] \cdot \\ &\left\{ -F_2(p) + \left( 1 / \chi_{33}^E \right) \left[ \begin{array}{l} d_{33} E_3(p) \\ -[\gamma / \text{sh}(\delta\gamma)] \left[ \begin{array}{l} \text{ch}(\delta\gamma) \Xi_2(p) \\ -\Xi_1(p) \end{array} \right] \end{array} \right] \right\}, \end{aligned}$$

where  $\chi_{33}^E = s_{33}^E / S_0$ .

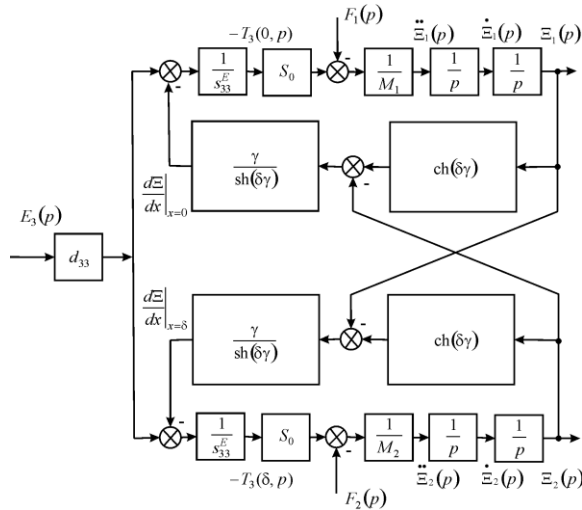


**Figure 2.** Parametric structural schematic diagram of a voltage-controlled piezoactuator for longitudinal piezoelectric effect

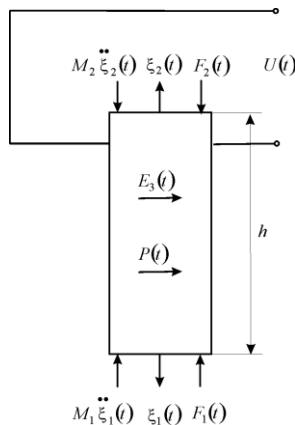


**Figure 3.** Piezoactuator for the transverse piezoelectric effect

In the equation (2) of the inverse transverse piezoeffect [12,14,15] are the following parameters:  $S_1 = \partial \xi(x, t) / \partial x$  is the relative displacement of the cross section along axis 1 Figure 3,  $d_{31}$  is the piezomodule for the transverse piezoeffect,  $s_{11}^E$  is the elastic compliance along axis 1,  $T_1$  is the stress along axis 1.

The solution of the linear ordinary differential equation (5) can be written as (6), where the constants C and B in the form

$$\begin{aligned} \Xi(0, p) &= \Xi_1(p) \text{ for } x=0, \\ \Xi(l, p) &= \Xi_2(p) \text{ for } x=h, \end{aligned} \quad (13)$$

$$\begin{aligned} C &= (\Xi_1 e^{h\gamma} - \Xi_2) / [2 \text{sh}(h\gamma)], \\ B &= (\Xi_1 e^{-h\gamma} - \Xi_2) / [2 \text{sh}(h\gamma)]. \end{aligned} \quad (14)$$

Then, the solution (5) can be written as

$$\Xi(x, p) = \left\{ \begin{array}{l} \Xi_1(p) \text{sh}[(h-x)\gamma] \\ + \Xi_2(p) \text{sh}(x\gamma) \end{array} \right\} / \text{sh}(h\gamma). \quad (15)$$

The equations of forces acting on the faces of the piezoactuator

$$T_1(0, p) S_0 = F_1(p) + M_1 p^2 \Xi_1(p) \text{ for } x=0, \quad (16)$$

$$T_1(h, p) S_0 = -F_2(p) + M_2 p^2 \Xi_2(p) \text{ for } x=h,$$

where

$$T_1(0, p) = \frac{1}{s_{11}^E} \left. \frac{d\Xi(x, p)}{dx} \right|_{x=0} - \frac{d_{31}}{s_{11}^E} E_3(p), \quad (17)$$

$$T_1(h, p) = \frac{1}{s_{11}^E} \left. \frac{d\Xi(x, p)}{dx} \right|_{x=h} - \frac{d_{31}}{s_{11}^E} E_3(p).$$

The set of equations describing the linear structural-parametric model and parametric structural schematic diagram of a voltage-controlled piezoactuator for transverse piezoelectric effect Figure 4

$$\begin{aligned} \Xi_1(p) &= \left[ 1 / (M_1 p^2) \right] \cdot \\ &\left\{ -F_1(p) + \left( 1 / \chi_{11}^E \right) \left[ \begin{array}{l} d_{31} E_3(p) \\ -[\gamma / \text{sh}(h\gamma)] \left[ \begin{array}{l} \text{ch}(h\gamma) \Xi_1(p) \\ -\Xi_1(p) \end{array} \right] \end{array} \right] \right\}, \quad (18) \end{aligned}$$

$$\begin{aligned} \Xi_2(p) &= \left[ 1 / (M_2 p^2) \right] \cdot \\ &\left\{ -F_2(p) + \left( 1 / \chi_{11}^E \right) \left[ \begin{array}{l} d_{31} E_3(p) \\ -[\gamma / \text{sh}(h\gamma)] \left[ \begin{array}{l} \text{ch}(h\gamma) \Xi_2(p) \\ -\Xi_1(p) \end{array} \right] \end{array} \right] \right\}, \end{aligned}$$

where  $\chi_{11}^E = s_{11}^E / S_0$ .

Let us consider the piezoactuator for the shift piezoelectric effect (2) on Figure 5.

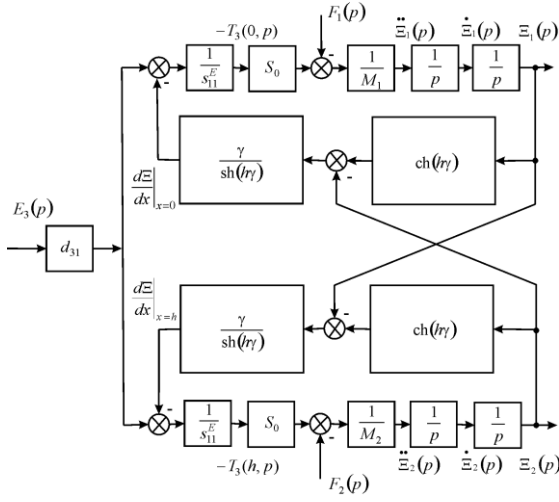


**Figure 4.** Parametric structural schematic diagram of a voltage-controlled piezoactuator for transverse piezoelectric effect

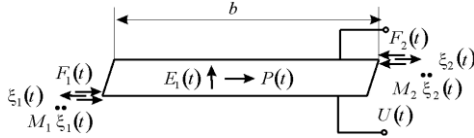


**Figure 5.** Piezoactuator for the shift piezoelectric effect

We obtain the following set of equations describing the structural-parametric model and schematic diagram Fig. 6

$$\Xi_1(p) = \left[ 1 / (M_1 p^2) \right] \cdot \left\{ -F_1(p) + \left( 1 / \chi_{55}^E \right) \begin{bmatrix} d_{15} E_1(p) \\ -[\gamma / \text{sh}(b\gamma)] \left[ \text{ch}(b\gamma) \Xi_1(p) \right] \end{bmatrix} \right\}, \quad (19)$$

$$\Xi_2(p) = \left[ 1 / (M_2 p^2) \right] \cdot \left\{ -F_2(p) + \left( 1 / \chi_{55}^E \right) \begin{bmatrix} d_{15} E_1(p) \\ -[\gamma / \text{sh}(b\gamma)] \left[ \text{ch}(b\gamma) \Xi_2(p) \right] \end{bmatrix} \right\},$$

where  $\chi_{55}^E = s_{55}^E / S_0$ .

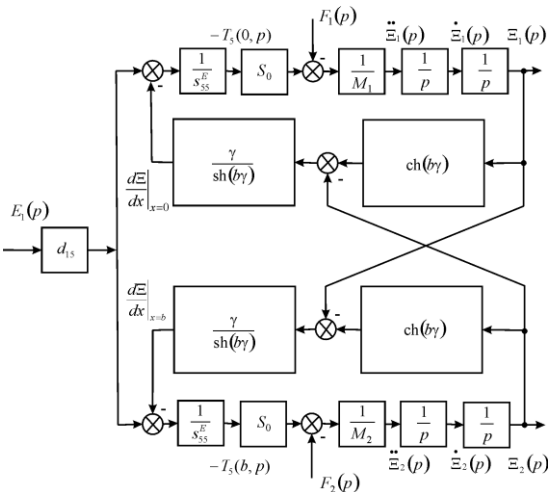


**Figure 6.** Parametric structural schematic diagram of a voltage-controlled piezoactuator for shift piezoelectric effect

From (2), (3), (12), (18), (19) we obtain the system of equations describing the generalized linear structural-parametric model of the electromagnetoelastic actuator for the mechatronics systems

$$\Xi_1(p) = \left[ 1 / (M_1 p^2) \right] \cdot \left\{ -F_1(p) + \left( 1 / \chi_{ij}^\Psi \right) \begin{bmatrix} v_{mi} \Psi_m(p) \\ -[\gamma / \text{sh}(l\gamma)] \left[ \text{ch}(l\gamma) \Xi_1(p) \right] \end{bmatrix} \right\}, \quad (20)$$

$$\Xi_2(p) = \left[ 1 / (M_2 p^2) \right] \cdot \left\{ -F_2(p) + \left( 1 / \chi_{ij}^\Psi \right) \begin{bmatrix} v_{mi} \Psi_m(p) \\ -[\gamma / \text{sh}(l\gamma)] \left[ \text{ch}(l\gamma) \Xi_2(p) \right] \end{bmatrix} \right\},$$

$$\chi_{ij}^\Psi = s_{ij}^\Psi / S_0, v_{mi} = \begin{cases} d_{33}, d_{31}, d_{15} \\ g_{33}, g_{31}, g_{15}, \Psi_m = \begin{cases} E_3, E_1 \\ D_3, D_1 \\ H_3, H_1 \end{cases} \\ d_{33}, d_{31}, d_{15} \end{cases}$$

$$s_{ij}^\Psi = \begin{cases} s_{33}^E, s_{11}^E, s_{55}^E \\ s_{33}^D, s_{11}^D, s_{55}^D \\ s_{33}^H, s_{11}^H, s_{55}^H \end{cases}, c^\Psi = \begin{cases} c^E \\ c^D \\ c^H \end{cases}, \gamma = \begin{cases} \gamma^E \\ \gamma^D \\ \gamma^H \end{cases}, l = \begin{cases} \delta \\ h \\ b \end{cases}$$

where the parameter  $\Psi$  of the control parameter for the electromagnetoelastic actuator:  $E$  for voltage control,  $D$  for current control,  $H$  for magnetic field strength control;  $s_{ij}^\Psi$  - elastic compliance at  $\Psi = \text{const}$ ;  $d_{33}, d_{31}, d_{15}$  - piezomodules;  $g_{33}, g_{31}, g_{15}$  - piezoelectric constants;  $c^\Psi$  - speed of sound at  $\Psi = \text{const}$ ;  $l$  - geometrical size in the deformation direction accordingly equal to  $\delta, h, b$  - thickness, height or width of the electromagnetoelastic actuator;  $S_0$  - area of the corresponding cross-section of the actuator.

On Figure 7 shows the generalized parametric structural schematic diagram of the electromagnetoelastic actuator corresponding to the set of equations (20) of the actuator for the mechatronics systems.

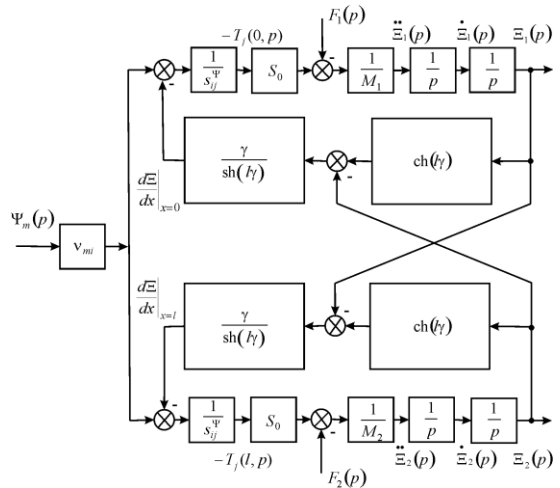


**Figure 7.** Generalized parametric structural schematic diagram of the electromagnetoelastic actuator

### 3. Transfer Functions of Electromagnetoelastic Actuator for Mechatronics Systems

We consider the construction of the transfer functions from the generalized structural-parametric model (20) of the electromagnetoelastic actuator for mechatronics systems.

After algebraic transformations of the generalized structural-parametric model of the actuator we provided the transfer functions of the actuator in matrix form [14-23], where the transfer functions are the ratio of the Laplace transforms of the displacement of the face actuator and the corresponding parameter or force at zero initial conditions.

$$\Xi_1(p) = W_{11}(p)\Psi_m(p) + W_{12}(p)F_1(p) + W_{13}(p)F_2(p), \quad (21)$$

$$\Xi_2(p) = W_{21}(p)\Psi_m(p) + W_{22}(p)F_1(p) + W_{23}(p)F_2(p),$$

where the generalized transfer functions of the electromagnetoelastic actuator are the following form:

$$\begin{aligned} W_{11}(p) &= \Xi_1(p)/\Psi_m(p) \\ &= v_{mi} \left[ M_2 \chi_{ij}^\Psi p^2 + \gamma \text{th}(l\gamma/2) \right] / A_{ij}, \end{aligned} \quad (22)$$

$$\begin{aligned} A_{ij} &= M_1 M_2 \left( \chi_{ij}^\Psi \right)^2 p^4 \\ &+ \left\{ (M_1 + M_2) \chi_{ij}^\Psi / \left[ c^\Psi \text{th}(l\gamma) \right] \right\} p^3 \\ &+ \left[ (M_1 + M_2) \chi_{ij}^\Psi \alpha / \text{th}(l\gamma) + 1 / \left( c^\Psi \right)^2 \right] p^2 \\ &+ 2\alpha p / c^\Psi + \alpha^2, \end{aligned}$$

$$\begin{aligned} W_{21}(p) &= \Xi_2(p)/\Psi_m(p) \\ &= v_{mi} \left[ M_1 \chi_{ij}^\Psi p^2 + \gamma \text{th}(l\gamma/2) \right] / A_{ij}, \end{aligned} \quad (23)$$

$$\begin{aligned} W_{12}(p) &= \Xi_1(p)/F_1(p) \\ &= -\chi_{ij}^\Psi \left[ M_2 \chi_{ij}^\Psi p^2 + \gamma / \text{th}(l\gamma) \right] / A_{ij}, \end{aligned} \quad (24)$$

$$\begin{aligned} W_{13}(p) &= \Xi_1(p)/F_2(p) = \\ W_{22}(p) &= \Xi_2(p)/F_1(p) = \left[ \chi_{ij}^\Psi \gamma / \text{sh}(l\gamma) \right] / A_{ij}, \end{aligned} \quad (25)$$

$$\begin{aligned} W_{23}(p) &= \Xi_2(p)/F_2(p) \\ &= -\chi_{ij}^\Psi \left[ M_1 \chi_{ij}^\Psi p^2 + \gamma / \text{th}(l\gamma) \right] / A_{ij}. \end{aligned} \quad (26)$$

Therefore, we obtain from equations (21) the generalized matrix equation for the electromagnetoelastic actuator

$$\begin{pmatrix} \Xi_1(p) \\ \Xi_2(p) \end{pmatrix} = \begin{pmatrix} W_{11}(p) & W_{12}(p) & W_{13}(p) \\ W_{21}(p) & W_{22}(p) & W_{23}(p) \end{pmatrix} \begin{pmatrix} \Psi_m(p) \\ F_1(p) \\ F_2(p) \end{pmatrix}. \quad (27)$$

Let us find the displacement of the faces the electromagnetoelastic actuator in a stationary regime for

$\Psi_m(t) = \Psi_{m0} \cdot 1(t)$ ,  $F_1(t) = F_2(t) = 0$  and inertial load. The static displacement of the faces the electromagnetoelastic actuator  $\xi_1(\infty)$  and  $\xi_2(\infty)$  can be written in the form

$$\xi_1(\infty) = \lim_{t \rightarrow \infty} \xi_1(t) = \lim_{p \rightarrow 0} p W_{11}(p) \Psi_{m0} / p \quad (28)$$

$$= v_{mi} l \Psi_{m0} (M_2 + m/2) / (M_1 + M_2 + m),$$

$$\xi_2(\infty) = \lim_{t \rightarrow \infty} \xi_2(t) = \lim_{p \rightarrow 0} p W_{21}(p) \Psi_{m0} / p \quad (29)$$

$$= v_{mi} l \Psi_{m0} (M_1 + m/2) / (M_1 + M_2 + m),$$

$$\xi_1(\infty) + \xi_2(\infty) = \lim_{t \rightarrow \infty} (\xi_1(t) + \xi_2(t)) = v_{mi} l \Psi_{m0}, \quad (30)$$

where  $m$  is the mass of the electromagnetoelastic actuator,  $M_1, M_2$  are the load masses.

Consider a numerical example of the calculation of static characteristics of the piezoactuator from piezoceramics PZT at  $m \ll M_1$  and  $m \ll M_2$ . For  $d_{33} = 4 \cdot 10^{-10}$  m/V,  $U = 125$  V,  $M_1 = 10$  kg and  $M_2 = 40$  kg we obtain the static displacement of the faces of the piezoactuator  $\xi_1(\infty) = 40$  nm,  $\xi_2(\infty) = 10$  nm,  $\xi_1(\infty) + \xi_2(\infty) = 50$  nm.

The static displacement the faces of the piezoactuator for the transverse piezoelectric effect and inertial load at  $U(t) = U_0 \cdot 1(t)$ ,  $E_3(t) = E_{30} \cdot 1(t) = (U_0/\delta) \cdot 1(t)$  and  $F_1(t) = F_2(t) = 0$  can be written in the following form:

$$\xi_1(\infty) = d_{31}(h/\delta) U_0 (M_2 + m/2) / (M_1 + M_2 + m), \quad (31)$$

$$\xi_2(\infty) = d_{31}(h/\delta) U_0 (M_1 + m/2) / (M_1 + M_2 + m), \quad (32)$$

$$\xi_1(\infty) + \xi_2(\infty) = d_{31}(h/\delta) U_0. \quad (33)$$

Consider a numerical example for the calculation of static characteristics of the piezoactuator from PZT under the transverse piezoeffect at  $m \ll M_1$  and  $m \ll M_2$ . For  $d_{31} = 2.5 \cdot 10^{-10}$  m/V,  $h = 4 \cdot 10^{-2}$  m,  $\delta = 2 \cdot 10^{-3}$  m,  $U = 250$  V,  $M_1 = 10$  kg and  $M_2 = 40$  kg we obtain the static displacement of the faces of the piezoactuator  $\xi_1(\infty) = 1$   $\mu$ m,  $\xi_2(\infty) = 0.25$   $\mu$ m,  $\xi_1(\infty) + \xi_2(\infty) = 1.25$   $\mu$ m. The experimental and calculated values for the actuator are in agreement to an accuracy of 5%.

For the description of the piezoactuator for the longitudinal piezoelectric effect for one rigidly fixed face of the transducer at  $M_1 \rightarrow \infty$  we obtain from equation (23) and (26) the transfer functions  $W_{21}(p)$  and  $W_{23}(p)$  of the piezoactuator for the longitudinal piezoelectric effect in the following form

$$\begin{aligned} W_{21}(p) &= \Xi_2(p)/E_3(p) \\ &= d_{33} \delta / \left[ M_2 \delta \chi_{33}^E p^2 + \delta \gamma \text{cth}(\delta \gamma) \right], \end{aligned} \quad (34)$$

$$\begin{aligned} W_{23}(p) &= \Xi_2(p)/F_2(p) \\ &= -\delta \chi_{33}^E / \left[ M_2 \delta \chi_{33}^E p^2 + \delta \gamma \text{cth}(\delta \gamma) \right]. \end{aligned} \quad (35)$$

Accordingly, the static displacement  $\xi_2(\infty)$  of the piezoactuator under the longitudinal piezoeffect in the form

$$\xi_2(\infty) = \lim_{t \rightarrow \infty} \xi_2(t) = \lim_{p \rightarrow 0} pW_2(p)U_0/p = d_{33}U_0, \quad (36)$$

$$\xi_2(\infty) = \lim_{p \rightarrow 0} pW_{23}(p)F_0/p = -\delta s_{33}^E F_0/S_0. \quad (37)$$

Consider a numerical example for the calculation of static characteristics of the piezoactuator for longitudinal piezoeffects. For  $d_{33} = 5 \cdot 10^{-10}$  m/V,  $U = 100$  V we obtain  $\xi_2(\infty) = 50$  nm. For  $\delta = 6 \cdot 10^{-4}$  m,  $s_{33}^E = 3.5 \cdot 10^{-11}$  m<sup>2</sup>/N,  $F_0 = 400$  N,  $S_0 = 1.75 \cdot 10^{-4}$  m<sup>2</sup> we obtain  $\xi_2(\infty) = -48$  nm.

Let us consider the operation at low frequencies for the piezoactuator with one face rigidly fixed so that  $M_1 \rightarrow \infty$  and  $m \ll M_2$ . Using the approximation of the hyperbolic cotangent by two terms of the power series in transfer functions (34) and (35), at  $m \ll M_2$  we obtain the expressions in the frequency range of  $0 < \omega < 0,01c^E/\delta$

$$W_{21}(p) = \Xi_2(p)/E_3(p) = d_{33}\delta / (T_t^2 p^2 + 2T_t \xi_t p + 1), \quad (38)$$

$$\begin{aligned} W_{23}(p) &= \Xi_2(p)/F_2(p) \\ &= -\left(s_{33}^E \delta / S_0\right) / (T_t^2 p^2 + 2T_t \xi_t p + 1), \end{aligned} \quad (39)$$

$$T_t = \left(\delta / c^E\right) \sqrt{M_2/m} = \sqrt{M_2/C_{33}^E},$$

$$\xi_t = (\alpha\delta/3) \sqrt{m/M_2}, C_{33}^E = S_0 / (s_{33}^E \delta) = 1 / (\chi_{33}^E \delta),$$

where  $T_t$  is the time constant and  $\xi_t$  is the damping coefficient,  $C_{33}^E$  - is the rigidity of the piezoelectric actuator for  $E = \text{const}$  under the longitudinal piezoelectric effect.

In the static mode of operation the piezoelectric actuator for elastic load we obtain the equation for its displacement in the following form

$$\xi_2 = \frac{\xi_{2m}}{1 + C_e/C_{33}^E}, \quad (40)$$

where  $\xi_2$  is the displacement of the piezoactuator in the case of the elastic load,  $\xi_{2m} = d_{33}U_0$  is the maximum displacement of the piezoactuator,  $C_e$  is the load rigidity.

From (38), (40) we obtain the transfer functions of the piezoactuator with a fixed end and elastic inertial load

$$W_2(p) = \frac{\Xi_2(p)}{U(p)} = \frac{d_{33}}{(1 + C_e/C_{33}^E) (T_t^2 p^2 + 2T_t \xi_t p + 1)}, \quad (41)$$

where the time constant  $T_t$  and the damping coefficient  $\xi_t$  are determined by the formulas

$$\begin{aligned} T_t &= \sqrt{M_2 / (C_e + C_{33}^E)}, \\ \xi_t &= \alpha\delta^2 C_{33}^E / \left(3c^E \sqrt{M(C_e + C_{33}^E)}\right). \end{aligned}$$

At low frequencies the experimental and calculated the time constants for the piezoactuators are in agreement to an accuracy of 5%, for example, for the piezoactuator with one face rigidly fixed and elastic inertial load so that  $M_1 \rightarrow \infty$  and  $m \ll M_2$  for  $M_2 = 10$  kg,  $C_{33} = 9 \cdot 10^6$  N/m,  $C_e = 1 \cdot 10^6$  N/m we obtain  $T_t = 1 \cdot 10^{-3}$  s.

## 4. Results and Discussions

For mechatronics the structural-parametric model and the generalized linear parametric structural schematic diagram of the simple electromagnetoelastic actuator of the mechatronics systems are obtained taking into account equation of generalized electromagnetoelasticity (piezoelectric, piezomagnetic, electrostriction, and magnetostriction effects) and decision wave equation.

The results of constructing the generalized structural-parametric model and the generalized parametric structural schematic diagram of actuator for the longitudinal, transverse and shift deformations are shown in Figure 7.

The parametric structural schematic diagrams piezoelectric actuator for longitudinal, transverse, shift piezoelectric effects Figure 2, Figure 4, Figure 6 converts to the generalized parametric structural schematic diagram of the actuator for the mechatronics systems Figure 7 with the replacement of the following parameters:

$$\begin{aligned} \Psi_m &= E_3, E_3, E_1, \nu_{mi} = d_{33}, d_{31}, d_{15}, \\ s_{ij}^\Psi &= s_{33}^E, s_{11}^E, s_{55}^E, l = \delta, h, b. \end{aligned}$$

For the mechatronics systems it is possible to construct the generalized structural-parametric model, the generalized parametric structural schematic diagram and the transfer functions in matrix form of the electromagnetoelastic actuator, using the solutions of the wave equation of the actuator and taking into account the features of the deformations actuator along the coordinate axes.

The generalized linear structural-parametric model and the generalized parametric structural schematic diagram of the electromagnetoelastic actuator after algebraic transformations are produced the transfer functions of the electromagnetoelastic actuator for the mechatronics systems.

The piezoelectric actuator with the transverse piezoelectric effect compared to the piezoelectric actuator for the longitudinal piezoelectric effect provides a greater range of static displacement and a less working force and the magnetostriction actuators provides a greater range of static working forces for the mechatronics systems.

## 5. Conclusions

The parametric structural schematic diagrams and the transfer functions of the piezoactuators for the transverse, longitudinal, shift piezoelectric effects are obtained from linear structural-parametric models of the piezoactuators for the mechatronics systems.

The systems of equations are determined for the linear structural-parametric models of the piezoactuators for mechatronics. Using the obtained solutions of the wave equation and taking into account the features of the

deformations along the coordinate axes, it is possible to construct the generalized linear structural-parametric model and parametric structural schematic diagram of the electromagnetoelastic actuator for the mechatronics systems and to describe its dynamic and static properties.

The transfer functions in matrix form are described the deformations of the electromagnetoelastic actuator during its operation as a part of the mechatronics systems.

## References

- [1] Przybylski J. "Static and dynamic analysis of a flexensional transducer with an axial piezoelectric actuation," *Engineering structures*, 2015, 84, 140-151.
- [2] Afonin, S.M. "Solution of the wave equation for the control of an electromagnetoelastic transducer," *Doklady mathematics*, 73, 2, 307-313, 2006.
- [3] Afonin, S.M. "Structural parametric model of a piezoelectric nanodisplacement transducer," *Doklady physics*, 53, 3, 137-143, 2008.
- [4] Ueda J., Secord T., Asada H. H. "Large effective-strain piezoelectric actuators using nested cellular architecture with exponential strain amplification mechanisms," *IEEE/ASME Transactions on Mechatronics*, 2010, 15, 5, 770-782.
- [5] Karpelson, M., Wei, G.-Y., Wood, R.J. "Driving high voltage piezoelectric actuators in microrobotic applications," *Sensors and Actuators A: Physical*, 2012, 176, 78-89.
- [6] Schultz J., Ueda J., Asada H. *Cellular Actuators*. Oxford: Butterworth-Heinemann Publisher, 2017. 382 p.
- [7] Uchino, K. *Piezoelectric actuator and ultrasonic motors*. Boston, MA: Kluwer Academic Publisher, 1997, 347 p.
- [8] Gu G.-Y., Yang M.-J., Zhu L.-M. "Real-time inverse hysteresis compensation of piezoelectric actuators with a modified Prandtl-Ishlinskii model," *Review of scientific instruments*, 2012, 83, 6, 065106.
- [9] Talakokula V., Bhalla S., Ball R.J., Bowen C.R., Pesce G.L., Kurchania R., Bhattacharjee B, Gupta A., Paine K. "Diagnosis of carbonation induced corrosion initiation and progression in reinforced concrete structures using piezo-impedance transducers," *Sensors and Actuators A: Physical*, 2016, 242, 79-91.
- [10] Yang, Y. , Tang, L. "Equivalent circuit modeling of piezoelectric energy harvesters," *Journal of intelligent material systems and structures*, 20, 18, 2223-2235, 2009.
- [11] Cady, W.G. *Piezoelectricity an introduction to the theory and applications of electromechanical phenomena in crystals*. New York, London: McGraw-Hill Book Company, 1946, 806 p.
- [12] *Physical Acoustics: Principles and Methods*. () Vol.1. Part A. Methods and Devices. Ed.: W. Mason. New York: Academic Press, 1964, 515 p.
- [13] Zwillinger, D. *Handbook of Differential Equations*. Boston: Academic Press, 1989, 673 p.
- [14] Afonin, S.M. "Structural-parametric model and transfer functions of electroelastic actuator for nano- and microdisplacement, Chapter 9 in *Piezoelectrics and Nanomaterials: Fundamentals, Developments and Applications*. Ed. I.A. Parinov. New York: Nova Science, 2015, pp. 225-242.
- [15] Afonin, S.M. "Generalized parametric structural model of a compound electromagnetoelastic transducer," *Doklady physics*, 50, 2, 77-82, 2005.
- [16] Afonin, S.M. "Parametric structural diagram of a piezoelectric converter," *Mechanics of solids*, 37, 6, 85-91, 2002.
- [17] Afonin, S.M. "Parametric block diagram and transfer functions of a composite piezoelectric transducer," *Mechanics of solids*, 39, 4, 119-127, 2004.
- [18] Afonin, S.M. "Static and dynamic characteristics of a multy-layer electroelastic solid," *Mechanics of solids*, 44, 6, 935-950, 2009.
- [19] Afonin, S.M. "Design static and dynamic characteristics of a piezoelectric nanomicrotransducers," *Mechanics of solids*, 45, 1, 123-132, 2010.
- [20] Afonin, S.M. "Electroelasticity problems for multilayer nano- and micromotors," *Russian engineering research*, 31, 9, 842-847, 2011.
- [21] Afonin, S.M. "Absolute stability conditions for a system controlling the deformation of an electromagnetoelastic transducer," *Doklady mathematics*, 74, 3, 943-948, 2006.
- [22] Afonin, S.M. "Generalized structural-parametric model of an electromagnetoelastic converter for nano- and micrometric movement control systems: III. Transformation parametric structural circuits of an electromagnetoelastic converter for nano- and micromovement control systems," *Journal of computer and systems sciences international*, 45, 2, 317-325, 2006.
- [23] Afonin, S.M. "Block diagrams of a multilayer piezoelectric motor for nano- and microdisplacements based on the transverse piezoeffect," *Journal of computer and systems sciences international*, 54, 3, 424-439, 2015.
- [24] *Springer Handbook of Nanotechnology*. Ed. by B. Bhushan. Berlin, New York: Springer, 2004, 1222 p.
- [25] *Encyclopedia of Nanoscience and Nanotechnology*. Ed. by H. S. Nalwa. Calif.: American Scientific Publishers. 10 Volumes, 2004.

# Unified Field Theory - 1. Universal Topology and First Horizon of Quantum Fields

Wei Xu\*

11760 Sunrise Valley Dr. Suite 403, Reston, Virginia 20191, USA

\*Corresponding author: wxu@virtumanity.com

**Abstract** Evolution from the classical dynamics  $W = P$  to the spacetime interwoven  $W = P + iV$  of modern physics, this paper demonstrates the yinyang physics of nature law: Universal Topology  $W = P \pm iV$ , that intuitively constitutes YinYang Manifolds and Dual Event Operations. Following the yinyang principle, its First Horizon naturally comes out with the YinYang Energy-State Equilibrium and YinYang Motion Dynamics, which replace the empirical “math law” and give rise to the general quantum fields to concisely include Schrödinger and Klein–Gordon Equations. As a result, this becomes a groundwork in the quest for Unified Physics: the workings of a life streaming of yinyang dynamics ...

**Keywords:** unified field theories and models, spacetime topology, quantum fields in curved spacetime, quantum mechanics, theory of quantized fields, field theory

**Cite This Article:** Wei Xu, “Unified Field Theory - 1. Universal Topology and First Horizon of Quantum Fields.” *International Journal of Physics*, vol. 5, no. 1 (2017): 16-20. doi: 10.12691/ijp-5-1-3.

## 1. Introduction

From *Euclidean* space to *Newtonian* mechanics introduced in 1687, the scientific approach known as classical physics seeks to discover the physical laws that mathematically describe the motion of bodies with a basic philosophy for *Physical Existence* of space and *Virtual Existence* of time, which has no manifold relationship of virtual and physical coordinates. Throughout this first generation of physics, the world  $W$  is interpreted by the physical function  $P(\mathbf{r}, t)$  using a spatial manifold  $M\{\mathbf{r}\}$  of three dimensions  $\mathbf{r}$ :

$$W = P(x_\mu, t) \quad (1.1a)$$

$$x_\mu \in M(\mathbf{r}) = \mathbf{r}\{x_1, x_2, x_3\} \quad (1.1b)$$

where time  $t$  is set as an independent parameter hidden to  $M\{\mathbf{r}\}$ .

As the second generation, modern physics couples the virtual  $V(x_\mu, t)$  and physical  $P(x_\mu, t)$  interweave into a single manifold  $M\{\mathbf{r} + i\mathbf{k}\}$ , known as *Minkowski* manifold [1], introduced in 1905.

$$W = P(x_\mu, t) + iV(x_\mu, t) \quad (1.2a)$$

$$x_\mu \in M\{r + ik\} = \{-ct, x_1, x_2, x_3\} \quad (1.2b)$$

where  $c$  is the speed of light. Although this model had advanced physical theories, it has diminished the virtual function  $\{i \cdot i \mapsto -1\}$  into a single physical manifold

$\{-ct, x_1, x_2, x_3\}$ , parallel to the *Lagrange* [3] density  $L = V - T$ . As a consequence, *Einstein*, *Schrödinger* *Klein* and *Gordon*, the greatest minds of the twentieth century, had to invent the *Math Laws* as a means of empirical approach to intuit their well-known theories of general relativity and quantum mechanics successfully.

Today, with acceptance of quantum mechanics, physics has reached a consensus on the existence of virtual supremacy. With the duality of both virtual and physical dynamics, this manuscript claims the following remarks as a groundbreaking in the unified physics:

1. Embedded in the well-known formulae, the nature reveals us the philosophical law of YinYang Topology in the forms of yin  $W = P + iV$  and yang  $W = P - iV$ , each functions as the complementary, inseparable and reciprocal opponent to the other. Together, they operates a life streaming of the interwoven dynamics.

2. The law intuitively comes out with YinYang Manifolds  $M\{\mathbf{r} \pm i\mathbf{k}\}$ , the conjugate coordinates with the dual complex vectors  $\mathbf{r} \pm i\mathbf{k}$ , which presents a groundbreaking in the spacetime manifolds.

3. Each of the manifold basis instinctively gives rise to a set of the conjugate Event Operators  $\partial_\mu \in \{\pm\partial_\kappa, \partial_r\}$  that replaces the empirical “math law” and ratifies the true philosophy to quantum mechanics.

4. With the operators, Yinyang Energy-State Equilibrium of First Horizon is reacted concisely as an infinite sum of series, elevating the meaning of a duality to Lagrangian density with its infinite accuracy beyond the second order of the traditional Energy Conservation.

5. The classic Motion Equation is boosted to play a vivid duality of yin and yang dynamics, which give rise to the first horizon: a pair of the general quantum fields, to

concisely include Schrödinger and Klein–Gordon equations, respectively.

As the outcome, this *Universal YinYang Topology* demonstrates the workings of the law towards the unified physics...

## 2. Universal Topology

Universe is the whole of everything in existence that operates under a system of topologically-ordered natural laws. This philosophy enlightens that the yin nature of physical  $P$  function is associated with its yang nature of virtual  $iV$  function to constitute a duality of the real world. In mathematics, it formulates the yinyang or complex-conjugate functions  $W^\pm(x^\mu)$  of one or more complex variables  $x^\mu$  in the neighborhood regime of every point in its universe domain  $G$ . This yinyang law, for example, is naturely embedded in the well-known formulae of (6.5), (7.3) and (7.4), which reveals the following expressions, named *Universal Topolog*

$$W^- = P + iV : W^-(x^\mu) \in G \quad (2.1a)$$

$$W^+ = P - iV : W^+(x^\mu) \in G \quad (2.1b)$$

where  $i$  marks an imaginary part as the conjugate of yinyang duality.

The *YinYang Topology* of equation (2.1) intuitively represents the yin and yang manifolds  $M\{\mathbf{r} \pm i\mathbf{k}\}$  as a set of global functions  $G$ , each composed of events  $\lambda$ , constituted by hierarchical structures of one coordinate yang manifold of vector  $\bar{\mathbf{q}}$  for virtual supremacy, and another coordinate manifold of yin vector  $\bar{\mathbf{q}}$  for physical supremacy. These principles convey that both manifolds operate simultaneously and transforming with their associated vector basis. In complex analysis, the global characteristics of  $W^\pm \in G(\lambda)$  are a set of holomorphic functions each with a dedicate manifold:

$$W^- = P(x^\mu, \lambda) + iV(x^\mu, \lambda) : x^\mu \in M\{\mathbf{r} \pm i\mathbf{k}\} \quad (2.2a)$$

$$W^+ = P(x^\mu, \lambda) - iV(x^\mu, \lambda) : x^\mu \in M\{\mathbf{r} - i\mathbf{k}\} \quad (2.2b)$$

$$\mathbf{r} = \{x_1, x_2, x_3\} \quad i\mathbf{k} = i\{ct, \dots\} \equiv \{x_0, \dots\} \quad (2.3)$$

$$dW^2 = dW^+ \cdot dW^- = g_{\mu\nu} dx^\mu dx^\nu \quad (2.4)$$

The virtual position of  $x_0 = ict$  naturally forms a conjugate duality of vectors for the real and imaginary coordinates and the dual event operators:

$$\bar{\mathbf{q}}\{+x_0, x_1, x_2, x_3\} = \mathbf{r} + i\mathbf{k} \mapsto \partial_\mu = \{\partial_{\kappa}^-, \partial_r\} \quad (2.5)$$

$$\bar{\mathbf{q}}\{-x_0, x_1, x_2, x_3\} = \mathbf{r} - i\mathbf{k} \mapsto \partial_\mu = \{\partial_{\kappa}^+, \partial_r\} \quad (2.6)$$

$$\partial_{\kappa}^\mp = \pm \mathbf{b}_0 \partial / \partial x_0 \quad \partial_r := \mathbf{b}_\alpha \partial / \partial x_\alpha \quad a \in \{1, 2, 3\} \quad (2.7)$$

where  $\mathbf{b}_0$  and  $\mathbf{b}_\alpha$  are the tetrad basis, a set of the operational symbols  $(\bar{\leftarrow}, \bar{\rightarrow})$  is defined for the virtual

manifold and other set of  $(\bar{\leftarrow}, \bar{\rightarrow})$  is defined for the physical manifold, shown in the Figure:

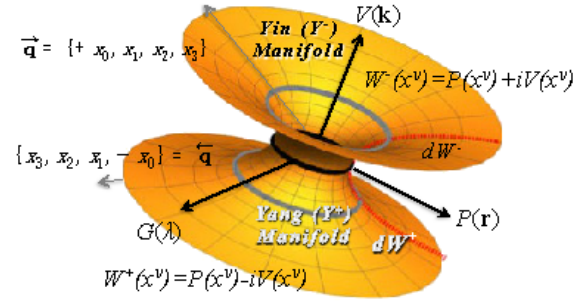


Figure 1. Universal YinYang Topology

Both manifolds simultaneously govern and alternatively perform the event operations as the unified dynamics. Exploring a yinyang duality of the virtual opponent  $\pm iV$ , we are entering a holistic world  $W = P \pm iV$  of the universe ...

From the yinyang equations of (2.1), the YinYang Topology represents a duality principle of physical and virtual functions:

$$P(x_\nu) = \frac{1}{2}[W^+(x_\mu) + W^-(x_\mu)] : W^\pm \subset W \quad (2.8)$$

$$V(x_\nu) = \frac{i}{2}[W^+(x_\mu) - W^-(x_\mu)] : W^\pm \subset W \quad (2.9)$$

Composed into a symmetric  $P(x_\mu)$ ,  $W^-$  is in physical primacy of yin dominant to the processes of formations or reproductions. Likewise, composed into an antisymmetric  $V(x_\mu)$ ,  $W^+$  is in virtual primacy of yang dominant to the processes of generations or annihilations. This means that the yinyang duality of  $W^\mp$  is the complementary opposition of inseparable and reciprocal pairs of all natural states.

Therefore, we have mathematically derived that the YinYang Topology of physical and virtual, space and time, or yin and yang manifolds presents the two-sidedness of any event, each dissolving into the other in alternating streams that form and operate horizons of life situations, movements, or actions through continuous helix-circulations in a universe topology, which lay behind the context of the main philosophical interpretation of quantum mechanics and beyond ...

## 3. YinYang Operations

In analysis of the operational functions  $f(\lambda)$  for an event  $\lambda$ , the first horizon involves the state densities  $\rho_\phi$ , space and time exposition  $\Gamma$ , and state entropy  $S_\psi$  towards the global equilibrium environment  $G$ . Assuming the energy state functions of  $\phi^-$  as yin states, and  $\phi^+$  as yang states, the state density  $\rho_\psi$  of the first horizon can be expressed by:

$$\rho_\phi = \phi^+(x^\mu, \lambda)\phi^-(x^\mu, \lambda) : x^\mu \in M\{\mathbf{r} \pm i\mathbf{k}\} \quad (3.1)$$

where the superscript signs of “-” and “+” indicate the yin and yang as a twin in equilibrium.

In a manifold, the entropy is a measure of the specific number of ways in which the manifold operations could be arranged towards either order or disorder. The state entropy  $S_\phi \in G$  can be written as the following, assuming the operational function  $f(\lambda)$  for the global property at an event  $\lambda$ :

$$dS_\phi = -k_s \int f(\lambda) \rho_\phi d\Gamma = \int L(\phi_n^-, \partial_\mu \phi_n^-, \phi_n^+, \partial_\nu \phi_n^+) d\Gamma \quad (3.2)$$

where  $k_s$  is a constant and  $L$  is an energy density. Apparently, it implies the event operation of  $\lambda$  is equivalent to the operator of  $\partial_\mu$ . Because of the complex manifolds, the conjugate vectors  $\bar{\mathbf{q}}$  and  $\bar{\mathbf{q}}$  of equations of (2.5) and (2.6) represent that an event  $\lambda$  has a conjugate pair of yinyang operators, shown as the following:

$$\partial_\mu \in \{\partial_{\kappa^-}, \partial_r\} \mapsto \partial_{\kappa^-} \phi_n^- = + \frac{\partial \phi_n^-}{\partial x_0}, \partial_r \phi_n^- := \nabla \phi_n^- \quad (3.3a)$$

$$\partial_\mu \in \{\partial_{\kappa^+}, \partial_r\} \mapsto \partial_{\kappa^+} \phi_n^+ = - \frac{\partial \phi_n^+}{\partial x_0}, \partial_r \phi_n^+ := \nabla \phi_n^+ \quad (3.3b)$$

A complex manifold yields a holomorphic function and is complex differentiable in a neighborhood of every point in its domain, such that an operational process can be represented as an infinite sum of terms that are calculated from any operator  $\lambda$  of the function's derivatives at an initial point  $\lambda_0$ , shown as the following

$$f(\lambda) = f(\lambda_0) + f'(\lambda_0)(\lambda - \lambda_0) + \dots \frac{f^n(\lambda_0)(\lambda - \lambda_0)^n}{n!} \quad (3.4)$$

known as the *Taylor* and *Maclaurin* series [4], introduced in 1715. Because the event process  $\lambda$  is operated in complex composition of the yinyang coordinates, it yields a linear function in a form of operational addition:  $f(\partial_{\kappa^-} + \partial_r) = f(\partial_{\kappa^-}) + f(\partial_r)$ , where the global vectors of each manifolds  $\{\mathbf{r} \pm i\mathbf{k}\}$  can constitute their orthogonal coordinate system  $\mathbf{r} \cdot \mathbf{k} = 0$ , respectively.

## 4. First Horizon of Energy Equilibrium

During yinyang dynamics, the first horizon density  $\phi_n^- \phi_n^+$  is incepted at  $\lambda_0 = 0$  by its yang evolution of  $\lambda = \partial_{\kappa^\pm}$ . This event evolution defines its yang operations on the energy state density in the form of kinetic energy density  $-T$ . The “-” sign represents the physical kinetics is a mirror or antisymmetric effect operated by the yang operation  $f(\partial_{\tau^-})$  of equation (3.4).

$$\begin{aligned} f(\partial_{\kappa^\pm}) (\phi_n^- \phi_n^+) &= \left( \frac{\kappa_\tau}{2} \partial_{\tau^\mp} + \kappa_{\tau 2} \partial_{\kappa^\pm}^2 + \dots \right) (\phi_n^- \phi_n^+) := \pm iT \\ &= \frac{\kappa_\tau}{2} \left( \frac{\partial \phi_n^-}{\partial x_0} \phi_n^+ - \phi_n^- \frac{\partial \phi_n^+}{\partial x_0} \right) \\ &= \kappa_{\tau 2} \left( \frac{\partial^2 \phi_n^-}{\partial x_0^2} \phi_n^+ - 2 \frac{\partial \phi_n^-}{\partial x_0} \frac{\partial \phi_n^+}{\partial x_0} + \phi_n^- \frac{\partial^2 \phi_n^+}{\partial x_0^2} \right) + \dots \end{aligned} \quad (4.1)$$

where  $\kappa_\tau$  and  $\kappa_{\tau 2}$  are coefficients of the first and second orders defined as the virtual state constants.

Considering the global event  $f(\lambda_0)$ , it operates on the timestate density to form the initial “local” energy  $\lambda_0$  as the internal energy density  $V_l$ , known as the potential  $V(\mathbf{r}, \lambda_0)$  of the system:

$$f(\lambda_0) (\phi_n^- \phi_n^+) = V(\mathbf{r}, \lambda_0) (\phi_n^- \phi_n^+) := V_l \quad (4.2)$$

Meanwhile, the yin function  $f(\partial_r)$  of the equation (3.4) at  $\lambda_0 = 0$  operates the event duality known as physical potential  $V_r$ :

$$\begin{aligned} f(\partial_r) (\phi_n^- \phi_n^+) &= (\kappa_r \nabla + \kappa_{r 2} \nabla^2 \dots) (\phi_n^- \phi_n^+) := V_r \\ &= \kappa_r \left( \nabla \phi_n^- \phi_n^+ + \phi_n^- \nabla \phi_n^+ \right) \\ &+ \kappa_{r 2} \left( \nabla^2 \phi_n^- \phi_n^+ + 2 \nabla \phi_n^- \nabla \phi_n^+ + \phi_n^- \nabla^2 \phi_n^+ \right) + \dots \end{aligned} \quad (4.3)$$

where  $\kappa_r$  and  $\kappa_{r 2}$  are coefficients of the first and second orders defined as the yin state constants.

With equations of (4.1)-(4.3), it has derived the First Horizon of Yinyang State-Energy Equilibrium in the following form:

$$L^\mp = V \pm iT = [f(\partial_{\kappa^\mp}) + f(\lambda_0) + f(\partial_r)] (\phi_n^- \phi_n^+) \quad (4.4)$$

which extends the yinyang meaning of the *Lagrangian* density, introduced in 1788. It demonstrates that the *Energy-State* at the first horizon is operated by the yinyang operations.

## 5. Yinyang Motion Conservations

As a natural principle, one entropy decreases and dominates the intrinsic yin development of virtual into physical horizon, while, at the same time, the opponent entropy increases and dominates the intrinsic yang annihilation of physical resources into virtual domain. Applying to the equation of (4.4), this principle represents Yin and Yang Motion Equations, respectively:

$$\partial_\mu \left( \frac{\partial L}{\partial (\partial_\mu \phi)} \right) - \frac{\partial L}{\partial \phi} = 0 \quad (5.1a)$$

$$L = \{L^-, L^+\}, \phi \in \{\phi_n^-, \phi_n^+\}, \partial_\mu \in \{\partial_{\kappa^\mp}, \partial_r\} \quad (5.1b)$$

Extends to the *Euler-Lagrange* [3] equation, introduced in the 1750s, for yinyang actions of any dynamic system, the new sets of the variables  $\phi$  and their operators  $\partial_\mu$  signify that yinyang manifolds maintains equilibria formulations from each of the entropy extrema, simultaneously driving a duality of yinyang fields giving rise to the first horizon of quantum dynamics, shown in the next few sections.

## 6. Yin Quantum Dynamics

Rising from the yang fields of  $\phi_n^+$  and  $\partial_\mu \phi_n^+$ , the dynamic reactions under yin manifold give rise to the

following motion equations of yin state fields  $\phi_n^-$  approximated at the first and second orders of perturbations from equations of (4.1)-(4.4) in term of the yin state equilibrium of  $L = (V_l + V_r) + iT$  :

$$\frac{\partial L}{\partial \phi_n^+} = V\phi_n^- + \kappa_r \nabla \phi_n^- + \kappa_{r2} \nabla^2 \phi_n^- + \frac{\kappa_\tau}{2} \frac{\partial \phi_n^-}{\partial x_0} + \kappa_{\tau 2} \frac{\partial^2 \phi_n^-}{\partial x_0^2} \quad (6.1a)$$

$$\partial_{\kappa^-} \left( \frac{\partial L}{\partial (\partial_\tau \phi_n^+)} \right) = -\frac{\kappa_\tau}{2} \frac{\partial \phi_n^-}{\partial x_0} - 2\kappa_{\tau 2} \frac{\partial^2 \phi_n^-}{\partial x_0^2} \quad (6.1b)$$

$$\nabla \left( \frac{\partial L}{\partial (\nabla \phi_n^+)} \right) = \kappa_r \nabla \phi_n^- + 2\kappa_{r2} \nabla^2 \phi_n^- \quad (6.1c)$$

Upon these interwoven relationships, the yinyang motion equation of (6.1) determines a linear partial differential equation of the state function  $\phi_n^-$  under the yin supremacy of physical dynamics:

$$3\kappa_{\tau 2} \frac{\partial^2 \phi_n^-}{\partial x_0^2} + \kappa_\tau \frac{\partial \phi_n^-}{\partial x_0} - \kappa_{r2} \nabla^2 \phi_n^- + V(\mathbf{r}, x_0) \phi_n^- = 0 \quad (6.2)$$

giving rise to the following *Yin Quantum Equation* from each of the respective opponents during their virtual interactions:

$$-\frac{3\hbar^2}{2\mu} \frac{\partial^2 \phi_n^-}{c^2 \partial t^2} - i\hbar \frac{\partial \phi_n^-}{\partial t} + \hat{H} \phi_n^- = 0 \quad (6.3a)$$

$$\kappa_\tau = \hbar c, \kappa_{\tau 2} = \kappa_{r2} = \frac{\hbar^2}{2m^*} \quad (6.3b)$$

where  $\hbar$  is the *Planck* constant [7], introduced in 1900,  $m^*$  is the reduced mass, and  $\hat{H}$  is defined as the relationship known as *Hamiltonian* [4], introduced in 1834 [5]. For the first order of the internal energy and kinetic-energy, equation (6.3) emerges as the *Schrödinger* equation [6] introduced in 1926, in the form of:

$$i\hbar \frac{\partial \phi_n^-}{\partial t} = \hat{H} \phi_n^- : \hat{H} \equiv \frac{-\hbar^2}{2m^*} \nabla^2 + V(\mathbf{r}, x_0) \quad (6.4)$$

It represents the manifold dynamics as the function of yin fields rises from its opponent in the yang interactions during the first horizon of timespace evolutions.

As an evidence of duality operation, consider  $N$  oscillators of quantum objects in the yin manifold. Developed by Paul Dirac, the "ladder operator" method allows us to extract effectively the energy eigenvalues as the following [3]:

$$H = \hbar\omega \sum_{i=1}^N \left( a_i^\pm a_i^\mp \pm \frac{1}{2} \right) \quad (6.5a)$$

$$\hat{a}_i^\mp = \sqrt{\frac{m\omega}{2\hbar}} \left( r_i \pm \frac{i}{m\omega} P_i \right) \quad (6.5b)$$

where  $\hat{a}_i^-$  is the operator for wave-mass of yin reproduction, while  $\hat{a}_i^+$  is the operator for mass-wave of yang annihilation. Both of the operators simultaneously

perform a duality of the virtual and physical reality of photons, which obey the law of *Universal Topology* - a *life streaming* of interwoven dynamics:  $W = P \pm iV$ .

## 7. Yang Quantum Dynamics

Rising from the yin fields of  $\phi_n^-$  and  $\partial_\mu \phi_n^-$  in parallel fashion, the dynamic reactions of the yang manifold give rise to the following motion equations of yang fields  $\phi_n^+$  approximated at the first and second orders of perturbations from equations of (4.1)-(4.4) in term of universal yang stae equilibrium  $L = (V_l + V_r) - iT$  :

$$\frac{\partial L}{\partial \phi_n^-} = V\phi_n^+ + \kappa_r \nabla \phi_n^+ + \kappa_{r2} \nabla^2 \phi_n^+ - \frac{\kappa_\tau}{2} \frac{\partial \phi_n^+}{\partial x_0} + \kappa_{\tau 2} \frac{\partial^2 \phi_n^+}{\partial x_0^2} \quad (7.1a)$$

$$\partial_{\kappa^+} \left( \frac{\partial L}{\partial (\partial_\tau \phi_n^-)} \right) = -\frac{\kappa_\tau}{2} \frac{\partial \phi_n^+}{\partial x_0} + 2\kappa_{\tau 2} \frac{\partial^2 \phi_n^+}{\partial x_0^2} \quad (7.1b)$$

$$\nabla \left( \frac{\partial L}{\partial (\nabla \phi_n^-)} \right) = \kappa_r \nabla \phi_n^+ + 2\kappa_{r2} \nabla^2 \phi_n^+ \quad (7.1c)$$

From these yinyang interwoven relationships, the motion equations of (5.1) determine a linear partial differential equation of the timestate  $\phi_n^+$ , giving rise to the following *Yang Quantum Equation* from each respective opponent during their yin interactions:

$$-\kappa_{\tau 2} \frac{\partial^2 \phi_n^+}{\partial x_0^2} - \kappa_{r2} \nabla^2 \phi_n^+ + \hat{V}(\mathbf{r}, x_0) \phi_n^+ = 0 \quad (7.2)$$

As a result, it represents the yinyang dynamics as the function of the yang fields rising from its opponent in the yin interactions during the first horizon of yinyang evolutions.

For a free particle, the energy is known as the *Einstein* equation [2]:  $\hat{V} \phi_n^+ = E \phi_n^+$ ,  $E = mc^2$ , introduced in 1905. This derives the following *Klein-Gordon* equation [3], introduced in 1928.

$$\frac{1}{c^2} \frac{\partial^2 \phi_n^+}{\partial t^2} - \nabla^2 \phi_n^+ + \left( \frac{mc}{\hbar} \right)^2 \phi_n^+ = 0 \quad (7.3a)$$

$$\kappa_{\tau 2} = \kappa_{r2} = \frac{\hbar^2}{m} = \frac{\hbar^2}{2m^*} \quad (7.3b)$$

Rewritten in form of the dual operations, it becomes the following:

$$\left( \hat{b}^+ \hat{b}^- + 1 \right) \phi_n^+ = 0 \quad (7.3c)$$

$$\hat{b}^\mp = \frac{\hbar}{mc} \left( i \frac{\partial}{\partial x_0} \pm \nabla \right) \quad (7.3d)$$

Demonstrating a duality of alternating actions, one operator  $\hat{b}^-$  is a yin process for physical reproduction, and another operator  $\hat{b}^+$  is a reverse yang process for

virtual annihilation. Hence, they comply with and are governed by the law of *Universal Topology*:  $W = P \pm iV$ .

For another example, equation of (7.3) represents the energy-momentum conservation in form of  $E^2 = W^-W^+$  as the following:

$$E^2 = (\mathbf{P}c + imc^2)(\mathbf{P}c - imc^2) \quad (7.4a)$$

$$-i\hbar\nabla \mapsto \mathbf{P}, -\hbar c\partial / \partial x_0 \mapsto E \quad (7.4b)$$

known as the relativistic equation relating any object's rest or intrinsic mass  $m$  with total energy  $E$  and momentum  $\mathbf{P}$ . It functions as the relativistic yinyang fields, representing the law of *Universal YinYang Topology* - a *life streaming* of yinyang interwoven dynamics:  $W^\mp = P \pm iV$ .

## 8. Conclusion

Governed by the *Universal Topology*  $W = P \pm iV$ , the law comes out intuitively with the first horizon of quantum mechanics, shown by the following remarks:

i) A duality of the yin and yang manifolds:

$$M \{ \mathbf{r} \pm i\mathbf{k} \} = \{ \pm x_0, x_1, x_2, x_3 \} : x_0 = ict \quad (8.1)$$

ii) A yinyang conjugate pair of event operations:

$$\partial_\mu \in \{ \partial_\kappa^\mp, \partial_r \} \mapsto \partial_\kappa^\mp \phi_n^\mp = \pm \frac{\partial}{\partial x_0} \phi_n^\mp, \partial_r \phi_n^\mp := \nabla \phi_n^\mp \quad (8.2)$$

iii) First Horizon of YinYang State Equilibrium:

$$L = \left[ V(x_\mu) + \frac{\hbar c}{2} \partial_\mu + \frac{\hbar^2}{2m^*} \partial_\mu^2 + \dots \right] (\phi_n^- \phi_n^+) \quad (8.3)$$

iv) A duality of Yinyang Quantum Fields:

$$\frac{3\hbar^2}{2m^*c^2} \frac{\partial^2 \phi_n^-}{\partial t^2} + i\hbar \frac{\partial \phi_n^-}{\partial t} = \hat{H} \phi_n^- : \hat{H} \equiv \frac{-\hbar^2}{2m^*} \nabla^2 + V(\mathbf{r}, t) \quad (8.4)$$

$$\frac{1}{c^2} \frac{\partial^2 \phi_n^+}{\partial t^2} - \nabla^2 \phi_n^+ + \frac{m}{\hbar^2} V(\mathbf{r}, t) \phi_n^+ = 0 \quad (8.5)$$

From a duality of yinyang dynamics these formulations represent that YinYang Topology of manifolds and event operations gives rise to the first horizon of quantum mechanics.

## References

- [1] Minkowski 1907-1908, The Fundamental Equations for Electromagnetic Processes in Moving Bodies. pp. 53-111.
- [2] Einstein, A. (1905), "Ist die Trägheit eines Körpers von seinem Energieinhalt abhängig?", Annalen der Physik 18: 639-643.
- [3] Sakurai, J. J. (1967). Advanced Quantum Mechanics. Addison Wesley.
- [4] Hazewinkel, Michiel, ed. (2001), "Taylor series", Encyclopedia of Mathematics, Springer.
- [5] Hand, L. N.; Finch, J. D. (2008). Analytical Mechanics. Cambridge University Press.
- [6] Schrödinger, E. (1926). "An Undulatory Theory of the Mechanics of Atoms and Molecules" (PDF). Physical Review 28 (6): 1049-1070.
- [7] Planck, Max (2 June 1920), The Genesis and Present State of Development of the Quantum Theory (Nobel Lecture).

# Various Innovative Technologic Devices in Shipping Energy Saving and Diminish Fuel Consumption

Yaser Sharifi, Hassan Ghassemi, Hamid Zanganeh \*

Department of Maritime Engineerin, Amirkabir University of Technology, Tehran, Iran

\*Corresponding author: [gaseemi@aut.ac.ir](mailto:gaseemi@aut.ac.ir)

**Abstract** Fluctuating fuel prices and stricter emissions regulations levied by IMO are the leading factors influencing the maritime shipping industry over the past few years and made shipping companies, charterers and ship owners find ways to reduce and optimize fuel consumption. So it is very crucial to reduce bunker consumption and it can be considered from two points of views: reducing consumption by optimizing the ship construction such as hull, propeller and rudder of the ships or by reducing the operational costs of the ships through controlling the speed, optimizing routes and so on. Present paper is evaluating these two approaches about the reduction of the fuel consumption.

**Keywords:** *fuel consumption, energy saving, innovative techniques*

**Cite This Article:** Yaser Sharifi, Hassan Ghassemi, and Hamid Zanganeh, "Various Innovative Technologic Devices in Shipping Energy Saving and Diminish Fuel Consumption." *International Journal of Physics*, vol. 5, no. 1 (2017): 21-29. doi: 10.12691/ijp-5-1-4.

## 1. Introduction

Maritime transport is the backbone of international trade and the global economy. Around 80 percent of global trade by volume and over 70 percent of global trade by value are carried by sea and are handled by ports worldwide. These shares are even higher in the case of most developing countries. The world seaborne trade was estimated at 9.84 billion tons in terms of total goods loaded in 2014 [1]. In recent years, increased competition and global shipping downturn have been putting downward pressure on the revenues of shipping companies; at the same time, increased security regulations and bunker prices and strict environmental targets continued to increase their operating costs. The bunker cost constitutes a large proportion of the operating costs of a shipping company. For example, Ronen [2] points out that when bunker fuel price is around 500USD per ton, the bunker cost constitutes about three quarters of the operating cost of a large containership.

On the other hand, as Psaraftis and Kontovas [3] said the amount of bunker consumed by ships also determines the amount of gas emission including CO<sub>2</sub>, CH<sub>4</sub>, SOX, NOX and various other pollutants such as particular matter, volatile organic compounds and black carbon. The above gases have negative effect on global climate and also have undesirable health effects. Therefore IMO is currently considering many measures to reduce them such as IMO MARPOL 73/78 Annex VI. In view of strict regulations on CO<sub>2</sub> emission, tradable CO<sub>2</sub> emission schemes have been developed and applied, and current average contract price is about 8 Euros of CO<sub>2</sub> emitted [4]. To meet future regulations on emissions, shipping

companies must either reduce bunker consumption or use cleaner but more expensive bunker fuel, or purchase emission quota from other companies. So it is very crucial for companies to reduce bunker consumption and it can be considered from two points of views: reducing consumption by optimizing the ship construction such as hull, propeller and rudder of the ships or by reducing the operational costs of the ships through controlling the speed, optimizing routes and so on. This paper aims to develop ship fuel efficiency analysis from these two points of views and thus we review the existing literature on bunker fuel efficiency with issues such as sailing speed and voyage optimization and also ships structure and hydrodynamic optimizations.

About the ship structure optimization and its effect on the fuel consumption, DSME energy saving devices [5], ABS ship energy efficiency measures advisory [6] and ABS seminar by Soren Hansen [7] provides guidance to owners and operators, on a wide range of options being promoted to improve vessel efficiency, reduce fuel consumption and lower emission through description of new technologies, their limitations and applicability or effectiveness.

Operational costs of ship mainly related to bunker costs and the sailing speed is one of the main determinants of the fuel consumption rate of a ship. The quantitative relationship between a ship's fuel consumption rate and sailing speed is the basis for speed optimization and it has studied by Wang and Meng [8], Kontovas and Psaraftis [3]. Natteboom and Carriou [9] based on 2259 container ships studied the effect of speed on fuel consumption. A higher sailing speed generally means a shorter transit time and fewer ships required to maintain a fixed, e.g. weekly service frequency. Sailing speed optimization is therefore closely related to a wide class of issues in liner shipping

network analysis, schedule design, service frequency determination, specifically studied by Catalani [10]. Ronen [3] propose cost models for analyzing the relationship between bunker prices, sailing speed, service frequency and number of ships on a shipping rout. Pyörre [11] discussed the challenges of speed on each leg of a voyage.

Despite the fruitful achievements regarding sailing speed optimization, studies on liner shipping network analysis seldom touch on the influence of the environment (wind, wave and currents) on ship's fuel consumption. Wang and Meng [12] were aware of possible influence of bad weather in ship schedules, but do not provide a quantitative relationship between fuel efficiency and weather condition. In fact, most of existing studies on the effect of environment on ship's fuel efficiency deal with environmental routing problem especially the weather routing problem. As Chen [13], Roh [14] and Safaei et al. [15] showed in their studies, rout selection is concerned with choosing a fair sailing track from the origin port to the destination port, by taking into account all severe factors effecting the fuel consumption such that desired objectives or combination of them are optimized. Generally an environmental routing system should balance the objectives of safety, fuel consumption, emissions and ship schedules. One of the main difficulties in doing so is the uncertainties of environmental information that make the problem complicated.

## 2. Optimizing Fuel Consumption through Optimizing of Ship Structure

The best measures for a ship to improve efficiency differ to a great extent depending upon ship type, cargoes, routes and other factors. The difficulty is in determining which ones are most appropriate for a particular vessel and service. Here we will review some perspectives of energy efficiency through optimizing ship structure.

Hull form optimization continues to be recognized as a growing field within the marine community as a means to improve energy efficiency of ships. Here we will review some benchmarks for assessing efficiency, describe the methods available to today's naval architect for optimizing hull form and propeller, and outline some of the issues that owners should consider in the assessment of the hull form aiming to enhance vessel fuel efficiency.

### 2.1. Optimizing Ship Particulars

#### 2.1.1. Ship Size – Capacity

For containerhips, increasing size from 4,500 TEU to 8,000 TEU reduces fuel consumption for propulsion by about 25 percent (measured in terms of fuel consumption per ton/nm of cargo transported). Increasing from 8,000 to 12,500 TEU reduces consumption by about 10 percent. The largest savings occur for higher speed ships and are most significant for smaller sized vessels. Increasing size from 4,500 TEU to 8,000 TEU reduces construction cost in terms by about 15 percent (measured in terms of USD per TEU). This shows transport efficiency in terms of fuel consumption per ton/mile of cargo moved for

containerhips as a function of capacity in TEUs. A service speed of 22.5 knots is assumed for all designs. The cargo payload is determined assuming stowage of 7 ton/TEU average weight containers within the constraints of slot capacity, available deadweight, container securing restrictions and visibility limits.

#### 2.1.2. Service Speed

For containerhips of 4,500 TEU and above, reducing speed by 1 knot reduces propulsion fuel consumption by 12 to 15 percent. For oil tankers, reducing speed by 1 knot reduces fuel consumption by 17 to 22 percent.

When selecting the service speed for liner services, customer expectations and the need for regularity of service should also be introduced into the study. For charter markets, the variability in charter rates should be accounted for, which tends to encourage a higher service speed so revenues can be maximized when rates are high. If the only focus of designing for slower speeds is low fuel consumption or low EEDI, the result may be low powered ships that may not operate safely in heavy seas or maneuver and stop safely. Such low powered ships may seem economically attractive at first, but the owner and designer should guard against such designs. Because of these concerns the issue of a minimum power requirement is being addressed by IMO.

Designing for the right speed, or right range of speeds, has other benefits as well. A hull form optimized for the slower speed usually means a fuller form and higher cargo deadweight. It is also possible to refine the hull form for multiple drafts and possibly multiple speeds if cargo quantities may vary or there are significant ballast legs. The main engine and propeller can be optimized around the slower speed for maximum benefit.

#### 2.1.3. Principal Dimensions

Increasing the length/beam ratio or increasing length and reducing the block coefficient can provide reductions in propulsion fuel consumption up to 3 to 5 percent. As compared to increasing beam or depth, length is the more expensive dimension. For example, increasing L/B on an Aframax tanker from 5.5 to 5.75 while holding the ship speed and cargo volume constant increases construction cost by roughly 0.25 to 1 percent.

Increasing the length while reducing the beam and maintaining the draft, displacement and block coefficient ( $C_b$ ) constant typically yields improvements in hull efficiency, provided additional ballast is not needed to maintain adequate stability. A higher length/beam ratio tends to reduce wave making resistance, while the reduced beam/draft ratio tends to reduce wetted surface and therefore the frictional resistance.

## 2.2. Minimizing Hull Resistance and Increasing Propulsion Efficiency

Propulsion fuel reductions of 5 to 8 percent are anticipated through further optimization of hull forms and propellers. Optimization of the hydrodynamic performance of a vessel's hull form and propulsor in order to achieve the least required power and best propulsion efficiency involves several interrelated efforts:

- Optimization of the hull form given the principal particulars (lines development)
- Optimization of the propeller(s) for the flow from the hull and installed machinery
- Design and arrangement of the rudder in relation to the propeller and flow lines
- Study of optimal energy-saving devices.

### 2.2.1. Optimizing the Hull Form (Lines)

Viscous (frictional) resistance is the major component of overall resistance, accounting for between 70 and 93 percent of the total resistance in tankers and containerships. The percentage of total resistance attributed to viscous (frictional) resistance is greatest for slower, larger ships. Wave making resistance increases with ship speed and is a larger component of overall resistance for high-speed, fine-form ships than it is for slower, full form ships. When developing a full body hull form such as a tanker, emphasis is placed on reducing wetted surface as viscous resistance is such a major component of overall resistance. Another important consideration is to provide a smooth and gradual transition to the propeller, to avoid separation of flow at the stern and provide for a uniform wake field (i.e. constant axial velocities at each radius). This encourages the LCB to be as far forward as practical, although care must be taken to avoid a harsh shoulder forward. Mitigating wave propagation at the forward shoulder is more important than reducing wave making. Employing blunter bow shape is encouraged over finer bows. Blunt bows tend to accommodate a smoother transition. The blunter bow shape allows a shift in volume from the midship region into the forebody region, resulting in better overall resistance performance for full body ships.

### 2.2.2. Forebody Optimization

Forebody optimization includes consideration of the bulb design, waterline entrance, forward shoulder and transition to the turn of the bilge. Potential flow calculations are routinely applied in this optimization process.

The properly designed bulbous bow reduces wave making resistance by producing its own wave system that is out of phase with the bow wave from the hull, creating a canceling effect and overall reduction in wave making resistance.

### 2.2.3. Aftbody Optimization

Aftbody optimization includes efforts to mitigate stern waves, improve flow into the propeller and avoid eddy effects. A properly designed stern can reduce the aft shoulder crest wave as well as the deep wave trough and stern waves. Improving the nature of the stern flow can lead to improved propulsive efficiency. (Flow improving devices such as stern flaps may be beneficial).

Single screw sterns forward of the propeller may be V-shaped, U-shaped or bulb types. The tendency today is towards the bulb shape, as the improved wake reduces cavitation and vibration. Asymmetrical sterns are designed to improve propulsive efficiency through pre-rotation of the flow to the propeller and to some extent by reducing the thrust deduction. The pre-rotation of the flow into the

propeller helps reduce the separation of flow in the stern aft of the propeller. To date, these enhancements have not been proven to be sufficiently effective to offset the extra cost and complexity involved in construction, with the exception of some twin skeg designs.

### 2.2.4. Twin-skeg Design

Twin-screw propulsion arrangements offer enhanced maneuverability and redundancy, and are also adopted when the power required for a single propeller is excessive. Propulsion power may exceed what can be handled reasonably by a single propeller if, for example, the vessel design is draft limited and the propeller diameter is correspondingly reduced. For a twin screw design there is the choice of open shafts with struts or twin skegs (or gondolas).

For full-hull form ships, the Swedish testing facility SSPA has found that the twin skegs provides a 2 to 3 percent efficiency improvement over well optimized single screw designs with corresponding characteristics. If the propeller diameter on a single screw design is suboptimal due to draft restrictions, unloading of the propellers in twin skeg arrangements can lead to efficiency improvements of 6 percent or more.

### 2.2.5. Maneuvering and Course-keeping Considerations

A high block coefficient, forward LCB, lower length to beam ratio and open stern are factors that can lead to reduced directional stability. Accordingly, performance should be assessed through computation means or by model tests, either through captive tests in a towing tank or by free running model testing in an open basin. Where the vessel's operational requirements necessitate the use of a hull form with reduced directional stability, effective course-keeping can be provided by larger rudders, high performance rudders or skegs, which will induce a penalty in overall efficiency when compared to vessels not provided with such rudders or skegs. In such cases, viscous flow CFD assessment and model tests are recommended as the drag and added resistance resulting from the larger rudders, high performance rudders and skegs can vary substantially.

### 2.2.6. Added Resistance Due to Waves and Wind

There is a growing awareness among ship designers and ship owners of the importance of evaluating weather effects on performance throughout the design process. During the initial stage of design, consideration of wind and wave effects can influence ship proportions (increasing length/beam, reducing  $C_b$ , increasing freeboard, limiting bow flare). In particular, at higher sea states the added resistance in waves is a directly related to the ship's beam and waterplane shape. A more accurate assessment of sea margin, accounting for the behavior of the specific vessel and intended trade route will help determine the engine margin and propeller design point.

## 2.3. Energy-saving Devices

Many different devices have been studied to either correct the energy performance of suboptimal ship designs,

or to improve on already optimal or nearly-optimal standard designs by exploiting physical phenomena usually regarded as secondary in the normal design process, or not yet completely understood.

In this article we will have a look on a range of these devices, most of which historically concentrate on the improvement of propeller propulsion effectiveness. However, recent developments have led to a series of devices aimed at either reducing the hull frictional resistance or exploiting readily available natural resources, such as solar and wind energy. Some of these devices are mentioned here.

### 2.3.1. Propulsion Improving Devices (PIDs)

0 to 5 percent reduction in propulsion fuel consumption can be attained through these devices and they are best suited to correct known existing hydrodynamic problems. These devices include the following ones:

**2.3.1.1. Wake Equalizing and Flow Separation Alleviating Devices:** In general, wake equalization and flow separation alleviating devices are features to improve the flow around the hull that were developed to obviate propeller problems and added ship resistance caused by suboptimal aft hull forms. As such, they are less effective when the ship geometry has been designed correctly, with an eye at optimizing the flow to the propeller and avoiding the generation of detrimental hydrodynamic effects such as bilge vortices. The most common wake equalization and flow separation alleviating devices are Grothues spoilers, Schneekluth ducts and stern tunnels.

**2.3.1.1.1. Grothues Spoilers:** Grothues spoilers are small curved triangular plates welded at the side of the hull in front of the propeller and above the propeller axis. Their function is to deflect downward the flow of water so that it is redirected horizontally in towards the propeller. Grothues originally proposed them to minimize/prevent the formation of keel vortices in the U-shaped sterns of full block coefficient ( $C_b$ ) ships (tankers and bulk carriers). However, tank testing provided some indication that they would also improve the efficiency of the propeller in view of the larger amount of water made available to the upper portion of the screw and lesser component of the incoming wake in the plane of the propeller disk (both wake equalization effects). In the best cases, spoilers might also provide a limited amount of additional thrust to the ship as a result of the redirection of vertical flow components in the horizontal direction.

**2.3.1.1.2. Wake Equalizing (Schneekluth) Ducts:** The purpose of wake equalizing ducts is similar to that of the Grothues spoilers, in the sense that both types of devices try to redirect flow to the upper portion of the propeller disk, thus homogenizing the wake and improving hull efficiency. However, unlike Grothues spoilers, Schneekluth ducts also accelerate the flow by means of the lift created by the aerofoil shape of the duct cross-section. The latter can be designed so that it is more forgiving to variations of the angle of attack than Grothues.

**2.3.1.1.3. Stern Tunnels:** Stern tunnels are horizontal hull appendages placed above and in front of the propeller disk that deflects water down towards the propeller. In most cases, these devices are retrofitted to reduce the wake peak effect of pronounced V-shaped sterns, thus reducing vibration.

### 2.3.2. Pre-swirl Devices

Pre-swirl devices are hydrodynamic appendages to the hull aiming to condition the wake flow so that a rotation opposite to that of the propeller is imposed on it, thus improving the angle of attack of the flow on the propeller blades over the entire disk. Also, the pre-swirl rotating flow counteracts the rotation flow induced by the propeller. As a result, the flow leaving the propeller disc can be made to contain minimum momentum in the circumferential direction, thus requiring less kinetic energy to produce thrust (Figure 1).

Pre-swirl devices have been designed and installed both as retrofits to existing ships and as an integral feature of newbuildings. Normally, they can be made to work in nonoptimal flows (the ducted type in particular) but they work best in already optimal nominal wakes. In this sense, they can be considered as fully complementary to other optimization approaches with the exception of nonsymmetrical stern lines. These devices may result in 2 to 6 percent reduction in propulsion fuel consumption and include pre-swirl fins and stators, pre-swirl stators with accelerating ducts, rudder thrust fins, post-swirl stators and asymmetric rudders, rudder bulbs, propeller boss cap fin and divergent propeller caps.



**Figure 1.** Pre-swirl stator ahead of the propeller cause to increase the thrust of the propeller

### 2.3.3. High-efficiency Propellers

Under the umbrella of 'high-efficiency propellers' there are a vast number of often significantly different devices, accommodating different needs on different ship types with 3 to 10 percent reduction in propulsion fuel consumption.

In general, larger diameter propellers with fewer blades operating at lower RPM are more efficient than smaller, faster counterparts, for a given required PE. However, this general principle is balanced by the need for reasonable propeller clearances, the nominal wake distribution behind a given hull form, and the need to match propeller and engine best performance. This type of optimization is done routinely at the design stage, when the principal propeller characteristics, and its detailed geometry is optimized to achieve best performance for the design speed and draft. Anyway, there are different types of

propellers including controllable pitch propellers, ducted propellers, propellers with end-plates and Kappel propellers, contra-rotating and overlapping propellers, podded and azimuthing propulsion that can not be explained in this article. Some of those augmented devices on the ship employed to increase the thrust and efficiency are given in [Table 1](#).

## 2.4. Skin Friction Reduction

Viscous resistance accounts for the great majority of the resistance of a hull moving through water. This is particularly true for slower ships, where the wave making resistance is small both in percentage of the total, and in absolute terms. However, even for faster ships (where wave making resistance can account for some 30 percent of the total or more) reducing viscous resistance is still extremely attractive since this force increases with the square of the ship speed, thus becoming the source of an important portion of the total power consumption of a ship.

By far the largest component of viscous resistance is skin friction. This simply depends on the ship's wetted surface, and the way it drags the water in touch with it and in its immediate surroundings, as the ship moves through it. To some extent, skin friction can be reduced by three methods: reducing the wetted surface (linear reduction), reducing speed (quadratic reduction) or improving the way the wetted surface interacts with the fluid it is in touch with. Reducing the speed and wetted surface are by far the easier and more effective ways to reduce skin friction. However, they both significantly affect ship operability. For this reason, a large amount of development has been dedicated through the years to improving hull-fluid interaction, either by changing the way fluid behaves (through its density, viscosity and boundary layer growth) or by improving the wetted area surface texture so that it would offer the best interaction with such fluid.

### 2.4.1. Air Lubrication

The general idea in air lubrication is to minimize the

power needed to force air to stay in touch with those parts of the hull that would normally be in contact with water. There are two main types of air lubrication. In air cavity systems, a thin sheet of air is maintained over the flat portions of a ship's bottom with the aid of pumps and hull appendages. In ideal conditions, this effectively amounts to a reduction in the wetted surface at the expense of the power needed to supply the pumps and the added resistance due to the hull modifications. An alternative method is that of effectively reducing the density and improving the viscous behavior of the water in contact with the hull by mixing it with air in the form of micro-bubbles.

There are some explanations that up to 10 percent reduction in propulsion fuel consumption can be attained through skin friction reduction.

### 2.4.2. Hull Surface Texturing

One method to reduce skin friction is to alter the way flow velocity grows through the boundary layer or the way the boundary layer grows along the hull. This depends in a complex way on ship speed and the geometrical characteristics (on all scales) of the hull. In general, a smooth hull surface is considered to be conducive of best performance and, to a large extent, this is the case when the alternative is a fouled hull as a consequence of marine growth. However, it has been demonstrated that some further benefits can be achieved by adopting particular types of surface texturing in place of a uniformly smooth hull. More specifically, the presence of riblets and semi-spherical micro cavities of certain sizes can distort the flow through the boundary layer and thus reduce skin friction.

This type of technology is still in its infancy and it is unclear how the correct shape and size of texture can be achieved and maintained on a ship's hull. However, some paints are being developed that might be able to achieve this in the future. The saving through this technology is unknown but it is not likely more than 5 to 10 percent reduction in propulsion fuel consumption. Drag reduction types are presented in [Table 2](#).

**Table 1. Types of energy saving devices**

Type of energy devices	Remarks
Aft body shape	Causes to increase the efficiency of the propulsor and also diminish the drag
Fore- body shape	Causes to diminish drag
Wake equalizing	Make uniform the flow into the propeller
Grothues spoilers	Deflect the flow and redirect it toward the propeller
Stern tunnels	Deflect the flow toward the propeller
Pre-swirl	Improving the angle of the attack of the flow on the propeller blades and thus requires less kinetic energy to produce thrust
Twin-skeg	enhancing maneuverability and redundancy, and also adopted when the power required for a single propeller is excessive

**Table 2. Types of drag reduction**

Type of drag reduction	Remarks
Hull Surface Texturing	Causes to increase efficiency and decreasing friction through distorting the flow
Reducing the speed	Causes to increase efficiency through decreasing resistance
Air cavity systems	Reducing the wetted surface and thus decreasing the drag
Micro-bubbles	Reducing the wetted surface and thus decreasing the drag

## 2.5. Renewable Energy

The utilization of renewable energy sources is currently benefiting from vast international attention in many industrial fields, including shipping. In our industry, attempts in this direction are naturally concentrating on wind power, since it is readily available at sea and has a history of successful use. However, photovoltaic (PV) solar panels are also being considered in specific fields such as the generation of auxiliary power.

### 2.5.1. Wind

Wind has been used to propel ships for the millennia, but the vast practical benefits of modern propulsion systems have meant the progressive decline and disappearance of sails from all merchant vessels. The feasibility of returning to sails needs to be integrated with the complexity of operation imposed by this type of propulsion.

However, the large fuel-saving benefits that wind power can provide estimated about 30 percent and should not be underestimated. Wind power seems to be reasonably easy to achieve in an effective way. Unfortunately, the technology commercially available at present is not advanced enough to achieve this aim. However, significant progress has been made during the last few years and it is reasonable to expect further improvements in the short term. In the following, the most promising technologies under development are discussed. [Figure 2](#) shows two especial types of the energy generated using wind and air venting.

**2.5.1.1. Towing Kites:** Towing kites are currently the only wind power technology commercially available to ships. The principle behind it is relatively simple, although the technology necessary to deploy, control and recover the kite is rather complex. In practice, extra power is provided to propel the ship by flying a kite tethered to

the vessel's bow. The kite speed through the air increases its efficiency compared to standard sails but the setup requires a computer to control the kite.

The real concern regarding towing kites is on the complexity of its operation and the risk associated with the system behavior in rough weather. As the largest gains provided by towing kites are when strong tail winds are present, it is paramount that the system can be operated safely, reliably and with no additional strain of the already limited crew resources available on board.

### 2.5.1.2. Rotor Sails, Flettner Rotors and Windmills:

Flettner rotors are vertical, cylindrical sails spinning around their axis, as shown in [Figure 3](#). A propulsive force is generated in the direction perpendicular to that of the wind hitting the rotor as a result of the Magnus effect. For this reason, rotor sails offer maximum efficiency near apparent beam wind conditions, a characteristic that could make them interesting as a complement to towing kites. However, rotors are normally powered by a diesel engine driven motor to achieve the necessary RPM. Also, unless they are made to telescopically collapse onto the deck to minimize aerodynamic drag when they are not in use, they might increase fuel consumption for a large range of wind directions. For these reasons, it is unclear if the overall efficiency of these systems can offer them a realistic chance of commercial success.

An alternative to powering the rotors using engines is the use of vertical axis (savonius) wind turbines or VAWTs. They show some degree of autorotation as a result of the Magnus effect like Flettner rotors, but rotate simply as the result of wind hitting the blades. The other advantage of VAWTs is they can be made to power electrical generators, thus obviating to the limitation of standard Flettner rotors when the wind is from the stern. To this day, limited research is available on the onboard use of these devices, though, making it hard to assess their feasibility in practice.

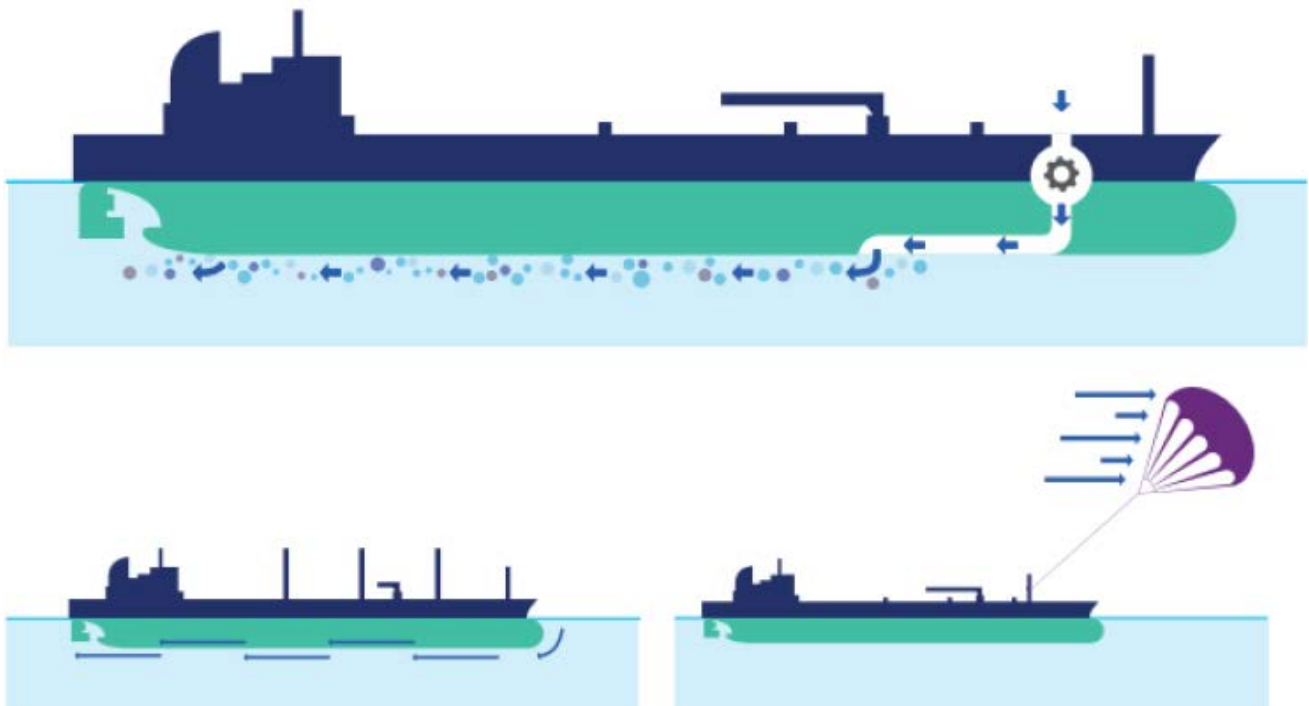


**Figure 2.** Energy generated using wind and air venting



**Figure 3.** Flettner rotors are vertical, cylindrical sails spinning around their axis

**2.5.1.3. Turbo sail:** Turbo sails were first proposed by Jacques-Yves Cousteau, Bertrand Charrier and Lucien Malavard as a way to significantly improve the efficiency of standard sails, thus limiting the size needed to power a vessel and their heeling effect. The principle is to use a fan

at the top of a hollow vertical cylinder to extract air from it. Inlets on the downwind side of the sail would then be opened to create a large depression and significantly increase lift.

Turbo sails were fitted on the *Alcyone* and operated in parallel with two standard diesel engines. An automatic system regulates the operation of the sails fan and the standard propulsion to optimize performance. Although this system is an interesting way to re-introduce wind propulsion in the modern shipping industry, very little public data is currently available on its actual performance.

### 2.5.2. Solar

There have been attempts to use PV panels to power small craft, such as the 30-m long catamaran *Planet Solar*, designed to circumnavigate the world on a 500 m<sup>2</sup> array. However, because of the low electrical output per unit surface, PV solar panels are better suited as an additional source of auxiliary power. In this role they have already been utilized on commercial vessels such as the NYK car carrier *Auriga Leader*, equipped with 328 solar panels at a cost of \$1.68 million. The energy generated by the 40 kW solar array on this ship is used to power lighting and other applications in the crew's living quarters (Figure 4). The obvious drawback of PV solar power is the high capital cost of these plants that have not yet benefited from large scale economies. It is to be hoped that as other land-based applications increase demand for this type of technology, the wider application in the shipping industry will be made viable. Table 3 presents three types of the marine renewable energy.



**Figure 4.** Energy generated using solar cell on the deck

**Table 3. Types of renewable energy**

Type of renewable energy	Remarks
Wind	Extra power is provided to propel the ship and causes to increase the propulsor efficiency
Solar	Can be used as additional source of auxiliary power
Wave	Many type are found to generate the energy (but not employed to the ship)

### 2.5.3. Compatibility

The devices presented in the renewable energy section are not always compatible with each other and might only be feasible for specific ship types or designs. In this part, an attempt is made to give guidance on the general applicability of each device. In reading the following, the reader should bear in mind that the stated compatibilities should always be verified by means of appropriate model tests or CFD analysis, since the correct functioning of nearly all of the above measures is strongly dependent on having a good understanding of the way they will interact with a given specific design.

## 3. Optimizing Fuel Consumption through Voyage Optimization

In the process of optimizing, the fuel consumption in a voyage many variables such as safety and security of the voyage, whether condition, wave conditions, currents, wind, the ship structural design, type and size of the ship, and speed all play a role and have different values and weighting factors. Voyage optimization is a technology to predict the ship performance in various sea states and current conditions, and based on the performance of the ship to assist ship masters in route selection. The targets of increasing energy efficiency and reducing Green House Gas (GHG) emission in the shipping industry can be achieved by voyage optimization. However, the practical and accurate prediction of ship operational performance is the prerequisite to achieve targets. The prepared operational performance model for each ship enables the user to investigate the relation between fuel consumption and the various sea states that the ship may encounter in its voyage. The potential results of operational performance model are collected in the ship operational performance database. Based on the database and real time climatological information, the ships' various courses can be evaluated according to a number of objectives including minimization of voyage time, maximization of safety, and minimization of fuel consumption using single or multi-objective methodologies. By utilizing a decision support tool, the ship's crew may now select the optimum course according to their preference.

Here we review some important and effective factors in fuel consumption during a voyage.

### 3.1. Route Selecting

It is clear that the optimum route is not the shortest one. In this respect, it is a competitive advantage for a charterer or ship owner to select the best route in terms of reduced fuel consumption, high safety and security of a passage. In order to do so, sea and whether condition must be considered by solving the maneuvering equations of a ship in a defined time domain for each ship who wants to sail

from point A to B. According to Safaei [15], a computer simulator showed a considerable decrease in fuel consumption of 3.7%. There are some challenges of route optimization and they will be discussed later on.

### 3.2. Speed Optimizing

Rising bunker costs and strict environmental targets are constraining voyage planning and driving technology solutions to address to these constraints by estimating journey times and speed requirements. By estimating optimal speed and route profiles based on empirical data and statistical models savings up to 10% can be achieved. Some companies have invested in software development that enables operators to compute, analyze and exploit real time data, adjusting performance dynamically based on the latest readings. These two factors are given in Table 4.

Speed optimization schemes face with tough challenges in daily vessel operations, due to strict itinerary demands and the limited accuracy of available whether and sea current forecasts. Since fuel-optimal routing is highly sensitive to constraints such as just-in-time arrival, one high-speed leg can wipe-out the accumulated fuel savings of an entire voyage. The optimization includes penalties for the undesired consequences of certain operating actions, such as excessive acceleration, as well as rewards for taking correct measures, such as maintaining a consistent speed, as appropriate. It is found that taking care to optimize speed can achieve possible  $3\pm 1\%$  energy saving.

The most important challenges in route and speed optimization include the following ones:

- *Quality of data*: It includes data correctness (validity), consistency, resolution and completeness (sufficiency)

- *Difficulty in estimating time of arrival accurately*: This is often subject to change and dependent on prevailing environmental conditions. Wave and weather impact the speed the vessel is able to travel.

- *Weather forecasting limitations*: Since it is still largely based on probability rather than accuracy, the reliability of any forecast needs to be included in the evaluation of the optimization results.

- *Sea current and weather forecasts*: Successful speed optimization relies heavily on accurate forecasts. Generally speaking, forecasts made on a global scale and provided by international centers do not take into account all of the specific characteristics of the local areas. This is also true of global sea current models when predicting conditions in costal environments. It is also worth saying that abundant data exist listing statistical long-term parameters of winds and waves on shipping routes. Wave size characterization might be contained in a typical atlas in a specific sea area and for a given season.

- *Off-design conditions for the vessel of propeller*: Care should be taken to optimize propeller use to avoid excess fuel consumption. For example, excessive acceleration can be avoided by reducing RPM variation.

Table 4. Navigation route

Type of navigation route	Remarks
Speed optimization	Causes to increase efficiency through reducing resistance and drag
Route selection	Causes to increase efficiency in addition to increase safety and security

- *Service speed optimization*: It is difficult to optimize the service speed obtained by a vessel in real weather condition when sailing on a given shipping route or indeed to support routing decisions in heavy seas.

- *Timely intervention*: Operators often have differing opinions on vessel operations and optimum setting based on their own experiences. This means detecting small changes in sea conditions is difficult to compute. On larger vessels, the control settings of variable parameters are typically adjusted on an hourly basis rather than minutes. A key challenge is to assist the operator in keeping the adjustments that impact energy consumption to a minimum while taking account of changes in the condition of the vessel and its environment at appropriate intervals.

- *User acceptance*: For a system providing operational assistance it is crucial to gain acceptance from the operator. This involves attaining some degree of confidence in using the man-machine-interface that informs and drives operational decision making. It depends particularly on ease-of-use, usefulness, and on adequate support provided to onboard decision makers.

- *Operation profile of the engine*: These profiles are complex and are impacted by changing engine operational characteristics due to partial loading conditions or technical degradation of the engine.

Speed optimization helps us to solve numerically the speed distribution during the voyage in a way that minimizes the amount of fuel consumed. In addition to avoiding excessive speed, the fuel consumption of the vessel can be reduced by continually monitoring any changes in engine load and weather conditions and making the necessary engine load adjustments as changes are detected. It is why accurate information about the state of the vessel and its environmental surroundings are important in maintaining an efficient operation. Since engine load is expressed in terms of power, engine RPM and torque are the key variables use to monitor fuel consumption. Additional factors such as density and caloric value of the fuel may be used to obtain more accurate modeling.

## 4. Conclusions

Maritime shipping has seen significant challenges over the past few years. Most notably, the introduction of the Ship Energy Efficiency Measurement Plan (SEEMP), the Energy Efficiency Design Index (EEDI) and Emission Control Areas (ECAs). As regulations add to the economic demands of shipping, the importance of ship fuel efficiency and voyage optimization is further amplified. Therefore companies recognize this and are

always seeking better ways to improve ship designing and vessel performance and operational efficiency through different ways. Here in this study we reviewed and extended a number of bunker consumption optimization methods including the following ones:

- a. Optimizing fuel consumption through optimizing of ship structure by optimizing ship particulars, minimizing hull resistance, increasing propulsion efficiency, using energy-saving devices, skin friction reduction and using renewable sources of energy
- b. Optimizing fuel consumption through voyage optimization by correct route selecting and optimizing ship speed.

## References

- [1] www.uctad.org
- [2] Ronen, D., *The effect of oil price on containership speed and fleet size* .Journal of the Operational Research Society, Vol. 62(1), pp. 211-216, 2011.
- [3] Kontovas, C., Psaraftis, H.N., *Reduction of emissions along the maritime intermodal container chain :operational models and policies*, Maritime Policy & Management, Vol. 38(4), pp. 451-469, 2011.
- [4] ICE-ECX, (2012).
- [5] Choi, Y, B., *DSME Energy Saving Devices for Greece SNAME*, 2008.
- [6] *ABS Ship energy efficiency measures advisory, status and guidance*.
- [7] Hansen, Soren, *Vessel Performance Management*, ABS SEMINAR, 2016.
- [8] Wang, S., Meng, Q., Liu, Z., *Bunker consumption optimization methods in shipping: A critical review and extensions*, Transportation Research Part, Vol. E53, pp.49-62, 2013.
- [9] Notteboom, T., Carriou, P., *Fuel surcharge practices of container shipping lines: is it about cost recovery or revenue making?* In: The 2009 International Association of Maritime Economists (IAME) Conference, Copenhagen, Denmark, 2009.
- [10] Catalani, Mauro., *Ship scheduling and routing optimization, An application to Western Mediterranean area*, European Transport \ Trasporti Europei, Vol. 42, pp. 67-82, 2009.
- [11] Pyörre, Jussi., *Overcoming the challenges in vessel speed optimization*, HANSA International Maritime Journal – 149. No. 9, Jahrgang, 2012.
- [12] Wang, S., Meng, Q., *Liner ship route schedule design with sea contingency time and port time uncertainty*, Transportation Research Part B46(5), pp. 615-633, 2012.
- [13] Chen, H., *Voyage Optimization Supersedes weather routing*, Jeppesen Commercial Marine Journal, 2013.
- [14] Roh, M.I., *Determination of an economical shipping rout considering the effects of sea state for lower fuel consumption*, Int. J. Naval Archit. Ocean Eng. 5. 2. pp. 246-262, 2013.
- [15] Safaei, A., Ghassemi, H., Ghiasi, M., *Voyage optimization for a very large crude carrier oil tanker, a regional voyage case study*, Scientific Journals of The Maritime University of Szczecin, 44(116) pp., 83-89, 2015.

# The Effect of Zr Concentration on Structural, Optical and Electrical Properties of $\text{Pb}(\text{Zr}_x\text{Ti}_{1-x})\text{O}_3$ PZT Prepared by Pulsed Laser Deposition Technique

Ghuson H. Mohammed<sup>1</sup>, Abdul Kareem D. Ali<sup>2</sup>, Hameed A. Radwan<sup>2,\*</sup>

<sup>1</sup>Department of Physics, University of Baghdad / College of Sciences

<sup>2</sup>Department of Physics, University of Tikrit/College of Education

\*Corresponding author: ham2348378@gmail.com

**Abstract**  $\text{Pb}(\text{Zr}_x\text{Ti}_{1-x})\text{O}_3$  PZT thin films with various ratio of Zr / Ti ( $x=0.1, 0.3, 0.5, 0.7, 0.9$ ) deposited on glass by pulsed laser deposition technique to investigate the structural, optical and electrical properties in these films. The films were deposited at room temperature. X-ray diffraction (XRD) analysis for PZT illustrated a perovskite phase with a polycrystalline structure at RT for all samples. Optical studies showed that the optical energy gap increases with increasing Zr concentration. The d.c. conductivity ( $\sigma_{d.c}$ ) decreased with increasing of Zr content. It was observed that the films have two activation energies that decrease with the increase of Zr content. Hall measurements showed that all the films were p-type and the carriers concentration were increase with the increasing of Zr, the mobility inversely proportional with the carriers concentration.

**Keywords:** Zr concentration, PLD technique,  $\text{Pb}(\text{Zr}_x\text{Ti}_{1-x})\text{O}_3$

**Cite This Article:** Ghuson H. Mohammed, Abdul Kareem D. Ali, and Hameed A. Radwan, "The Effect of Zr Concentration on Structural, Optical and Electrical Properties of  $\text{Pb}(\text{Zr}_x\text{Ti}_{1-x})\text{O}_3$  PZT Prepared by Pulsed Laser Deposition Technique." *International Journal of Physics*, vol. 5, no. 1 (2017): 30-36. doi: 10.12691/ijp-5-1-5.

## 1. Introduction

Discovery Semiconductors is one of the great scientific and technological advances of the 20th century, this has caused major economic change and may change our civilization [1]. Ferroelectric ceramic, dielectric hysteresis and non-linear behavior has been of interest since the 1950s, when these substances are found in the applications of various electronic devices [2]. An applications with a high range of user areas require future devices with more reduced size and power exhaustion, very-high speed, and high levels of implementation. To meet these challenges, we are in need to develop novel materials with improved qualities [3].

$\text{Pb}(\text{Zr}_x\text{Ti}_{1-x})\text{O}_3$  perovskite oxide is an attractive material due to its physical properties such as Ferroelectricity, piezoelectricity and high dielectric constant. These characteristics make PZT thin films are useful in a various applications such as microelectromechanical systems, magnetoelectric devices [4,5], fuel injection system in automobile industry, aerospace vibration control, energy harvesting from different vibration sources [6], sensors, infrared detectors, [7] and so on.

Different techniques are used to prepared PZT thin films [8,9], including both chemical and physical routes, such as plasma enhanced chemical vapor deposition, metal-organic chemical vapor deposition, sol-gel processing, evaporation, pulsed laser deposition and sputtering deposition, however, the properties of thin films

relay to some extent on the method of fabrication [9,10]. The most important deposition technique is PLD due its ability to transfer material compatibility from a multicomponent target to a growing film. PLD a promising technique for making thick film because it is offers the advantage of a high deposition rate. Because of High deposition rate in pulses, in addition to, mass transfer column erosion of solid thin films is improved. This allows sediment in the high growth temperatures, especially for epitaxial growth of volatiles [10,11]. The aim of the present work is to fabricate and analyze the thin films structural and morphological characteristics of  $\text{Pb}(\text{Zr}_x\text{Ti}_{1-x})\text{O}_3$  using PLD processing method.

## 2. Experimental Procedure

Bulk samples of  $\text{Pb}(\text{Zr}_x\text{Ti}_{1-x})\text{O}_3$  have been prepared by solid state reaction process. The powder of Lead dioxide, Zirconium dioxide and Titanium dioxide with a purity of 99.99% were Grinded and mixed together at a different concentration of ( $x = 0.1, 0.3, 0.5, 0.7, 0.9$ ) wt. % of the formula  $\text{Pb}(\text{Zr}_x\text{Ti}_{1-x})\text{O}_3$  in a mixture machine for (10 minute). After that it was pressed into pellets with (1.2 cm) diameter and (0.2 cm) thick, using hydraulic piston type (SPECAC), under the pressure of 6 tons/cm<sup>2</sup> for 10 minutes. The pellets were sintered in air to temperature (1073 K) for 2 hours then cooled to room temperature. The temperature of the furnace was raised at a rate of 250°C/hour.

The substrate used in this work for deposit of  $\text{Pb}(\text{Zr}_x\text{Ti}_{1-x})\text{O}_3$  thin films is the glass slides made in china

from "AFCO", with dimensions (75 × 25 × 1.2 mm). The substrate cleaned in the following steps:

1-The substrates were cleaned in distilled water to remove the impurities and residual Grime from the their surface.

2-The substrates were cleaned in alcohol by an ultrasonic system for 15 min in order to remove grease and some oxides, and dried by blowing air.

3-Eventually, The slides were wiped with soft paper.

The pulsed laser deposition experiment is fulfilled inside a vacuum chamber under (10<sup>-3</sup> mbar) vacuum conditions. The focused Nd:YAG laser beam at 800 mJ with a frequency second radiation at 1064 nm (pulse width 9 ns) frequency (6 Hz), for 400 laser pulses incident on the target surface makes an angle of 45° with it. The distance between the target and the laser gun is set to 15 cm, and between the target and the substrate is (2cm).

#### a. X-ray Diffraction analysis:

The structure of Pb(Zr<sub>x</sub>Ti<sub>1-x</sub>)O<sub>3</sub> alloys as mass and film by X-ray diffraction using a Philips X-ray diffraction system that records the intensity as a function of Bragg angle is investigated. The wavelength of the radiation source Cu Kα = 1.5405 Å, 20 mA current and the voltage was 30 kV. 2θ scan angle in the range (20-70) degree at 2cm.min<sup>-1</sup> speed. more interplane distance d (hkl) to various pages is determined using Bragg's law [12]:

$$n\lambda = 2d\sin\theta \quad (1)$$

Where n is the order of reflection.

lattice constants of relations estimate:

$$d = \frac{a}{(h^2 + k^2)^{1/2}} + \frac{c}{l} \quad (2)$$

Pb(Zr<sub>x</sub>Ti<sub>1-x</sub>)O<sub>3</sub> grain size (D) can be calculated using the Scherrer equation [13]:

$$D = K^* \lambda / \beta \cos\theta \quad (3)$$

Where: K\* is constant, θ the diffraction angle, β full width half maximum.

#### b. Optical Properties:

Optical properties of films with different content of Zr in Pb(Zr<sub>x</sub>Ti<sub>1-x</sub>)O<sub>3</sub> deposited on the glass at different room temperature (RT) at a wavelength of about 0.2 to 1.1 micrometers using UV / VIS Centra 5 spectrometer that previous GBC Scientific Equipment PTY LTD was. The spectrometer consists of two deuteriums and tungsten lamp light source at a wavelength of 190-390 nm and 390-1100 nm range of the spectrum. Data output wavelength, transmission and absorption in a computer program used to deduce the optical energy gap and the underlying edge optical and optical constant.

Fixed optical parameters are very important because they describe the optical behavior of materials. Energy absorption coefficient of a material is a function of photon energy band gap is very strong. Indicates a weakening of the incident photon energy absorption coefficient per unit thickness passing through a material. The main reason for this attenuation processes of absorption attributed [11,14]. Optical constants of refractive index (n), extinction coefficient (K), and real (ε<sub>r</sub>), and imaginary components (ε<sub>i</sub>) of the dielectric constant. The complex refractive index (n<sub>c</sub>) is defined as [15]:

$$n_c = n - iK. \quad (4)$$

It is related to the velocity of propagation (v), and light velocity(c) By:

$$v = \frac{c}{n_c}. \quad (5)$$

The refractive index can be calculated by formula [11]:

$$n = \left( \frac{4R}{(R-1)^2} - K^2 \right)^{1/2} - \frac{(R+1)}{(R-1)} \quad (6)$$

where R is the reflectance, and can be expressed by the relation [14]:

$$R = \frac{(n-1)^2 + K^2}{(n+1)^2 + K^2}. \quad (7)$$

Extinction coefficient that corresponds to the exponential decay of the wave as it passes through the material, as defined [11]:

$$K = \frac{\alpha\lambda}{4\pi} \quad (8)$$

(α) is given by:

$$\alpha = 2.303 \frac{A}{t} \quad (9)$$

Where A is the absorbance and t is the thickness of the film. The real and imaginary parts of the optical dielectric constant can be calculated using the following equation [15]:

$$(n - ik)^2 = \epsilon_r - \epsilon_i \quad (10)$$

where

$$\epsilon_r = n^2 - k^2 \quad (11)$$

and

$$\epsilon_i = 2nk. \quad (12)$$

#### c. Electrical properties:

Therefor the fundamental properties of semiconductor which determine its characteristics in addition to the width of energy gap, the mobilities of its charge carriers over a wide range of temperature. Thus the electrical properties of semiconductors are primarily interested and are dependent on the availability of holes in the valence band and electrons in the conduction band to facilitate the flow of charge under applied potential. Transport properties such as d.c electrical conductivity (σ<sub>d.c</sub>), Hall effect will be discussed in this section.

The resistivity (ρ) of the film is calculated using the following equation:

$$\rho = \hat{R} \cdot \hat{A} / L \quad (13)$$

Where  $\hat{R}$  is the sample resistance,  $\hat{A}$  is the cross section area of the films and L is the distance between the electrodes. The conductivity (σ<sub>d.c</sub>) of the film was determined from the relationship:

$$\sigma_{dc} = 1 / \rho. \quad (14)$$

The activation energy ( $E_a$ ) can be calculated from the plot of  $\ln\sigma$  versus  $1000/T$  according to equation

$$\sigma = \sigma_o \exp(-E_a / k_B T) \quad (15)$$

Where  $\sigma_o$  is the minimum electrical conductivity at 0K, T is the temperature and  $k_B$  are the Boltzmann's constant [16].

Hall is used to measure the semiconductor carrier concentration, mobility and it is used to detect whether a semiconductor is n or p- type.

When a constant current (I) below comes along x- axis from right to left in the presence of magnetic field(B) at z- axis with value (0.55T), the electron obeys Lorentz force in the beginning, and they drift toward the negative y- axis, and thus the sample surface charge too much and causing a transverse voltage. The Hall coefficient ( $R_H$ ) can be determined by measuring the Hall voltage ( $V_H$ ) that produces venues across the field by [17]:

$$R_H = \frac{V_H}{I} \cdot \frac{t}{B}. \quad (16)$$

From Hall coefficient equation, the semiconductor carrier concentration can be determined as given in the following:

$$R_H = \frac{1}{p \cdot e} \text{ For p - type} \quad (17)$$

$$R_H = \frac{-1}{n \cdot e} \text{ For n - type} \quad (18)$$

Where (e) is the charge of the electron. P and n is the carriers concentrations of holes and electrons respectively. If the conduction is due to one carriers type e.g. electrons:

$$\sigma_n = qn\mu_n \text{ For n - type.} \quad (19)$$

And for holes :

$$\sigma_p = qp\mu_p \text{ For p - type.} \quad (20)$$

We can measure the Hall Mobility as:

$$\mu_H = \frac{\sigma}{n \cdot e} \quad (21)$$

or

$$\mu_H = \sigma |R_H| \quad (22)$$

i.e., by knowing  $\sigma$ , the mobility can be determined.

### 3. Results and Discussion

#### a. Structural Measurements:

Figure 1 shows the XRD patterns obtained for  $Pb(Zr_x, Ti_{1-x})O_3$  thin films deposited on a glass substrate at RT and different concentration of (x= 0.1, 0.3, 0.5, 0.7, 0.9 wt. %). According to the International Center for Diffraction Data (ICDD), the structure of the thin films shows a polycrystalline tetragonal structure. It is obvious in the case of x= 0.1 and 0.3 reveals main peak along (101) which corresponding to  $2\theta = 31.5541^\circ$  and a small peaks along (100), (111) and (200) corresponding to  $2\theta = 22.6351^\circ$ ,  $29.2568^\circ$  and  $46.3514^\circ$  respectively, the perovskite phase is the dominant with a small impurity phases are formed. This impurity phases are decreased and the structure exhibit's more crystallization to be complete perovskite at x = 0.5 gain sharp intensity peak, at x=0.7 the reflections (100) and (001) disappear and appear (110) reflection corresponding to  $2\theta = 30.8784^\circ$  which indicate the change from tetragonal phase to rhombohedral phase [18]. Rhombohedral phase still the dominate perovskite structure at x = 0.7 and 0.9 with strong reflection (101) and a two weak reflections (110) and (201).

There are some shift in the peaks resulting from substituting Zr-ions instead of Ti-ions which is larger than Ti due to the variation of distance between the internal plane d [19]. using a computer program to calculate d-value from experimental work  $d_{exp}$ . and compare it with the standard values as given in ICDD card  $d_{std}$ . and find grain size by using Scherer's formula as shown in Table 1. After a simple comparison between  $d_{exp}$ . and  $d_{std}$ . it is found that the values of two parameter are identical which almost keep constant at light substitution of Zr x = 0.1, 0.3, 0.5 and gradually decrease at high substitution x = 0.7, 0.9.

**Table 1. Shows the peaks and its Bragg's angle, interplanar distance, and full width half at maximum for  $Pb(Zr_x, Ti_{1-x})O_3$  thin films at room temperature**

x	2 $\theta$ (Deg.)	FWHM (Deg.)	$d_{hkl}$ Exp.(Å)	G.S (nm)	$d_{hkl}$ Std.(Å)	hkl	card No.
0.1	21.6892	0.6081	4.0942	13.3	4.1560	(001)	96-901-1193
	22.6351	0.3378	3.9252	24.0	3.9050	(100)	96-901-1193
	31.5541	0.4730	2.8331	17.5	2.8459	(101)	96-901-1193
	32.2297	0.2027	2.7752	40.8	2.7613	(110)	96-901-1193
	39.2568	0.3379	2.2931	25.0	2.2999	(111)	96-901-1193
	46.3514	0.4730	1.9573	18.3	1.9525	(200)	96-901-1193
	57.1622	0.4054	1.6102	22.3	1.6100	(121)	96-901-1193
0.3	21.6892	0.5405	4.0942	15.0	4.1560	(001)	96-901-1193
	22.4324	0.5406	3.9602	15.0	3.9050	(100)	96-901-1193
	31.4189	0.8108	2.8450	10.2	2.8459	(101)	96-901-1193
	39.0541	0.5406	2.3045	15.6	2.2999	(111)	96-901-1193
0.5	21.7568	0.4730	4.0816	17.1	4.1560	(001)	96-901-1193
	22.4324	0.4054	3.9602	20.0	3.9050	(100)	96-901-1193
	30.2703	0.3379	2.9502	24.4	2.9613	(111)	96-500-0039
	31.2162	0.5406	2.8630	15.3	2.8459	(101)	96-901-1193
	50.2703	0.5405	1.8135	16.2	1.8134	(202)	96-500-0039
0.7	30.2703	0.3379	2.9502	24.4	2.9613	(111)	96-500-0039
	30.8784	0.4729	2.8935	17.4	2.8890	(110)	96-210-2946
	50.4054	0.8108	1.8090	10.8	1.8134	(202)	96-500-0039
0.9	30.2027	0.3379	2.9567	24.4	2.9613	(111)	96-500-0039
	50.3378	0.5406	1.8112	16.2	1.8134	(202)	96-500-0039

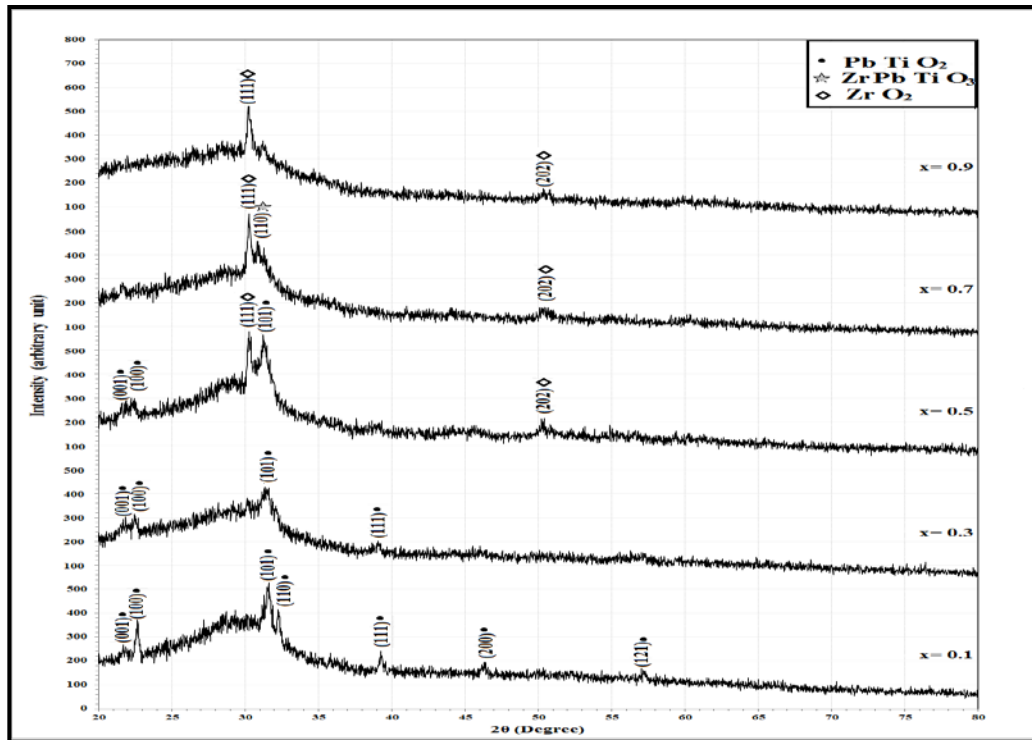


Figure 1. X-ray diffraction for  $\text{Pb}(\text{Zr}_x\text{Ti}_{1-x})\text{O}_3$  thin films with various value of  $x$  ( $x=0.1, 0.3, 0.5, 0.7, 0.9$ ) at room temperature

### b. Optical Measurements:

The transmittance spectrum as a function of wavelength in the range of (300-1100)nm of  $\text{Pb}(\text{Zr}_x\text{Ti}_{1-x})\text{O}_3$  thin films deposited at room temperature with different Zr content ( $x=0.1, 0.3, 0.5, 0.7, 0.9$ ). It is obvious from these figures and Table 2 that the transmittance is inversely proportional to concentration and that transmission increases with increasing of  $\lambda$  for all samples. Transmission decreases with increasing Zr content in  $\text{Pb}(\text{Zr}_x\text{Ti}_{1-x})\text{O}_3$ . It's clear that Zr content effect on the values of transmission. Also we can observe from Figure 2 that the transmission values are decrease with increasing of Zr content in  $\text{Pb}(\text{Zr}_x\text{Ti}_{1-x})\text{O}_3$  may be owing to increase in thickness of the film which cause the increase in absorption. In the other hand the decreasing of the transmission may be attributed to the creation of levels at the energy band by increasing thickness and this leads to the shift of peak to smaller energies, and this results agree with Khorsand [20]. Increasing Zr leads to increase the ratio of the large atoms resulting increase in thickness of samples and thereby increase in absorption which is in agreement with Puustinen [21].

Figure 3 show the absorption coefficient ( $\alpha$ ) as a function of wavelength ( $\lambda$ ) for  $\text{Pb}(\text{Zr}_x\text{Ti}_{1-x})\text{O}_3$  thin films. It can be observed from the figures that the values of absorption coefficient is higher ( $\alpha > 10^4$ ) $\text{cm}^{-1}$ , this is support to expect a direct electronic transition occurs in these region [22]. It is obvious that the absorption coefficient of the  $\text{Pb}(\text{Zr}_x\text{Ti}_{1-x})\text{O}_3$  films have a strong absorption coefficient at the shorter wavelength region and the absorption coefficient decrease at the long wavelength side. generally, absorption coefficient increase with the increasing of Zr concentration in the samples as shown in Table 2 and Figure 3.

The energy band gap decreases with increasing of Zr content in  $\text{Pb}(\text{Zr}_x\text{Ti}_{1-x})\text{O}_3$  as shown in Figure 4 and Table 2.  $E_g$  decreases from (3.41 to 3.21) eV with increasing the zr

content from (0.1 to 0.9) for RT, This decreasing of  $E_g$  with increasing of Zr content is attributed to the increase of the density of the localized states in  $E_g$  which result from lack in thickness of the membranes cause a shift to lower values of  $E_g$  for different content of Zr in  $\text{Pb}(\text{Zr}_x\text{Ti}_{1-x})\text{O}_3$ .

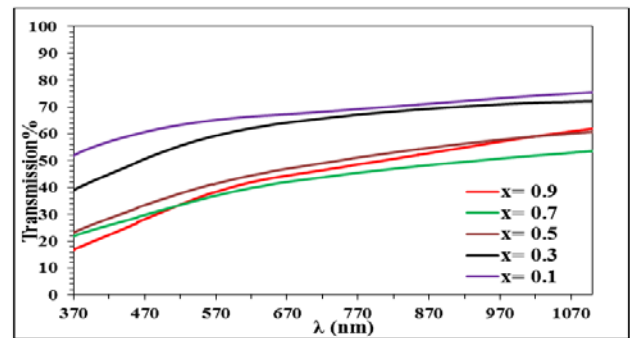


Figure 2. Transmittance spectrum as a function of wavelength for  $\text{Pb}(\text{Zr}_x\text{Ti}_{1-x})\text{O}_3$  films at RT and different concentrations of Zr

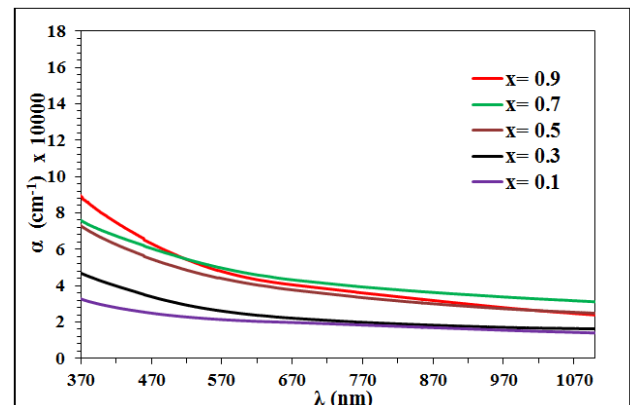


Figure 3. Absorption Coefficient as a function of wavelength for  $\text{Pb}(\text{Zr}_x\text{Ti}_{1-x})\text{O}_3$  films at RT and different concentrations of Zr

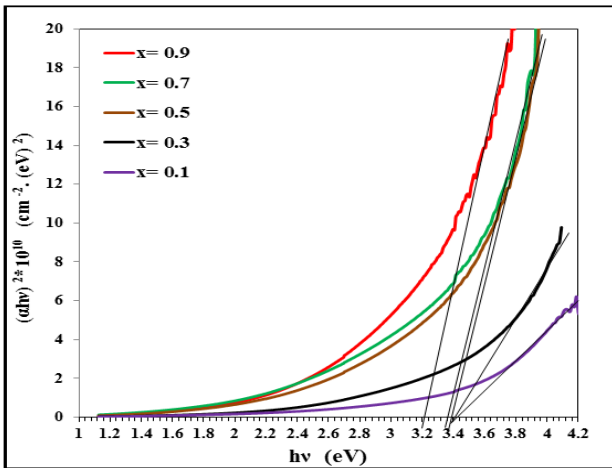


Figure 4.  $(\alpha hv)^2$  as a function of  $h\nu$  for  $Pb(Zr_xTi_{1-x})O_3$  films at RT and different concentration of Zr.

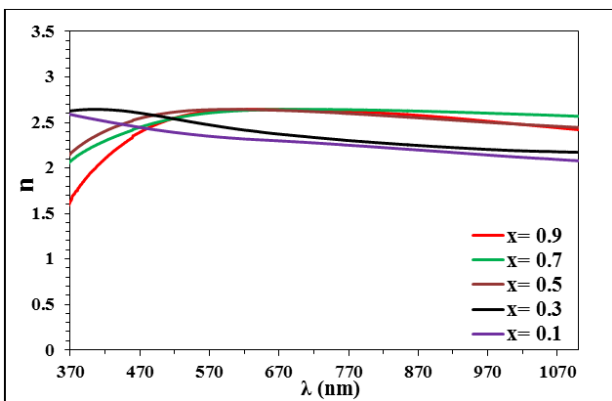


Figure 5. Refractive index as a function of wavelength for  $Pb(Zr_xTi_{1-x})O_3$  films at RT and different concentrations of Zr.

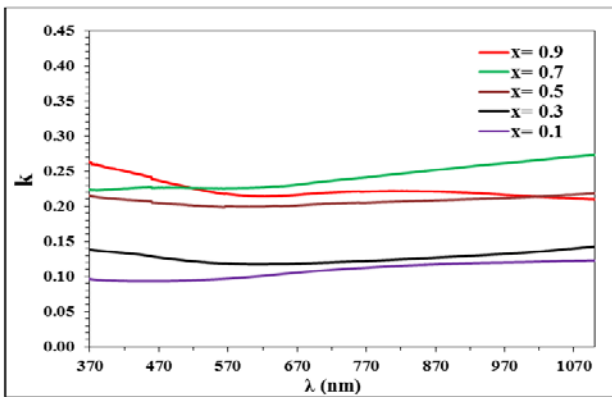


Figure 6. Extinction Coefficient as a function of wavelength for  $Pb(Zr_xTi_{1-x})O_3$  films at RT and different concentrations of Zr

Figure 5 show the refractive index increases with increasing the concentration of Zr. This behavior may be happen due to the increment in the energy gap which

cause expansion of the bond length in the lattice and decreases the defect which means decreasing of the reflection where the refractive index depends on it. The refractive values are increase from (2.33 to 2.64) at RT, this values are in agreement with Moret [23] and puustinen [21].

Figure 6 reveal the behavior of  $k$  is approximately similar to the corresponding absorption coefficient. It can be observe from this figure that the extinction coefficient increase with the increasing of Zr content in  $Pb(Zr_xTi_{1-x})O_3$  due to increment in thickness of the films.

The real and imaginary dielectric constants of thin films were plotted with different Zr concentration in  $Pb(Zr_xTi_{1-x})O_3$  at RT as shown in Figure 7 and Figure 8 respectively.  $(\epsilon_r)$  behavior is similar to the refractive index of less value because of  $k^2$  proportional to  $n^2$ , while  $(\epsilon_i)$  is mainly dependent on the value of  $k$ . The dielectric constants  $(\epsilon_r)$  and  $(\epsilon_i)$  are directly proportional to the Zr content in  $Pb(Zr_xTi_{1-x})O_3$  films as shown in Table 2.

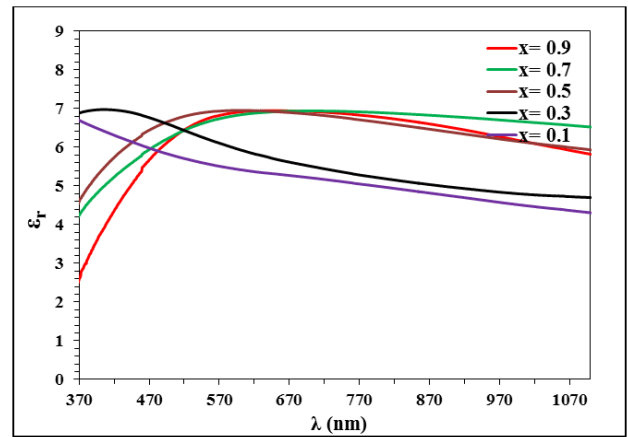


Figure 7. The variation of  $\epsilon_r$  with wavelength for  $Pb(Zr_xTi_{1-x})O_3$  films with different concentrations at RT

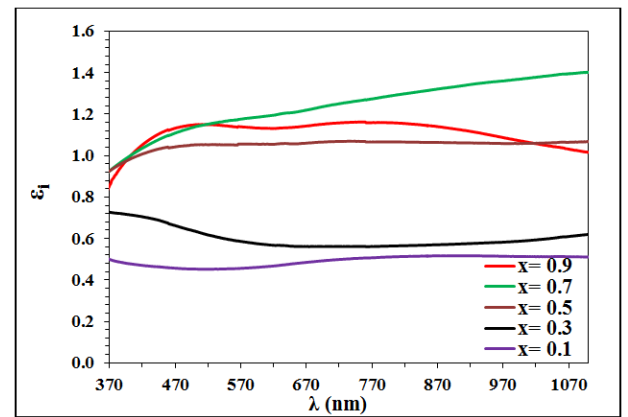


Figure 8. The variation of  $\epsilon_i$  with wavelength for  $Pb(Zr_xTi_{1-x})O_3$  films with different concentrations at RT

Table 2. Illustrates the transmission, absorption coefficient, energy band gap and optical constant at RT and different concentrations of Zr for  $Pb(Zr_xTi_{1-x})O_3$  thin films

Ta / K	x	T%	$\alpha$ (cm <sup>-1</sup> )	K	n	$\epsilon_r$	$\epsilon_i$	Eg (eV)
RT	0.1	66.02	20764	0.1	2.33	5.42	0.46	3.41
	0.3	61.13	24612	0.12	2.44	5.93	0.57	3.4
	0.5	43.39	41752	0.2	2.64	6.95	1.05	3.39
	0.7	38.8	47340	0.23	2.62	5.84	1.19	3.38
	0.9	40.7	44942	0.21	2.64	5.91	1.13	3.21

**c. Electrical Measurements:**

**DC conductivity**

It is clear from these figures that there are two activation energy  $E_{a1}$ ,  $E_{a2}$  and hence two transport mechanism were calculated using the relationship (12) of a slope tangent to logarithm conductivity  $\ln(\sigma)$  as a function of the inverted degrees of absolute temperature ( $1000 / T$ ) multiplied by the Boltzmann constant ( $k_B$ ) in units (eV) as shown in Figure 9. the energy gap in the scores of low-lying heat and produces a second activation energy ( $E_{a2}$ ) at high temperatures and in which transitions charge carriers in a manner stimulus or thermal irritability [22]. It was found that the activation energy values ( $E_{a1}, E_{a2}$ ) decrease with the increasing of Zr concentration as a result of decreases in the energy gap for all samples as shown in Table 3 and Figure 10. Table 3 illustrates obviously that the d.c. conductivity ( $\sigma$ ) increase with the increasing of concentration of Zr.

**Hall Effect**

The results of Hall effect reveal positive Hall coefficient (p-type charge carriers) for  $Pb(Zr_x, Ti_{1-x})O_3$  thin films i.e. Hall voltage increases with the increase of the current. Figure 11 and Figure 12 illustrate the variation of carriers concentration, Hall mobility of  $Pb(Zr_x, Ti_{1-x})O_3$  films with different Zr content at RT. It can be observed from these figures and Table 4 that the carriers concentration were directly proportional and the mobility is inversely proportional with the different concentration of Zr, this may be due to increase the number of valence electron which result from increase of atoms.

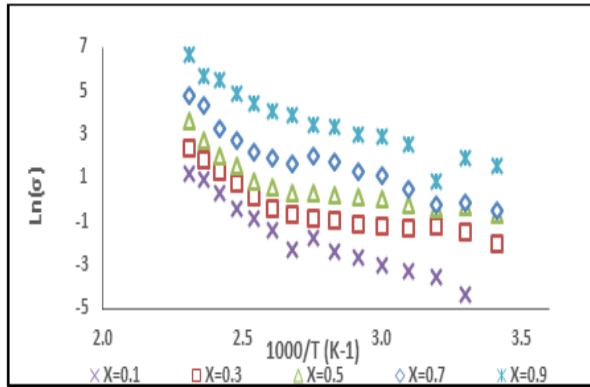


**Figure 9.**  $\ln\sigma$  versus  $1000/T$  for  $Pb(Zr_x, Ti_{1-x})O_3$  films with different x-concentration at RT

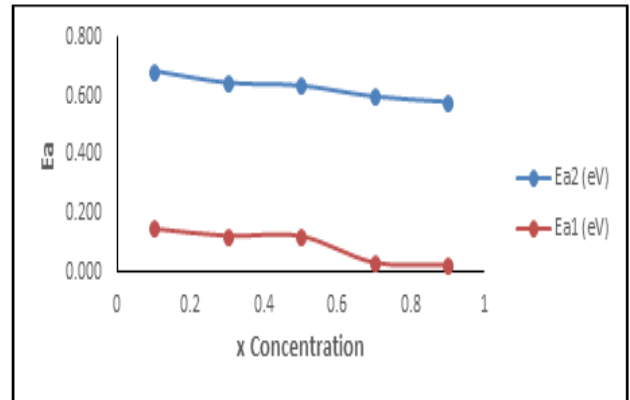


**Figure 10.** Variation of  $E_{a1}$  and  $E_{a2}$  for  $Pb(Zr_x, Ti_{1-x})O_3$  films with different x-concentration at RT

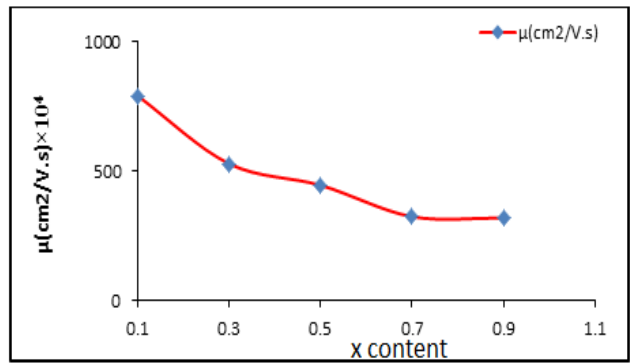


**Figure 11.** Variation of mobility for  $Pb(Zr_x, Ti_{1-x})O_3$  films with different x-concentration at RT

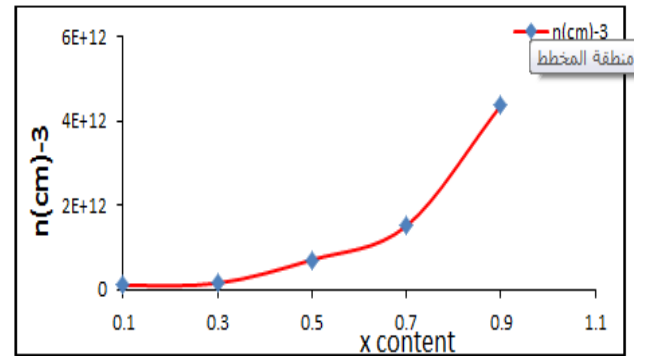


**Figure 12.** Variation of carrier concentration for  $Pb(Zr_x, Ti_{1-x})O_3$  films with different x-concentration at RT

**Table 3. DC activation energies, their ranges and conductivity for  $Pb(Zr_x, Ti_{1-x})O_3$  films with different Zr content at RT**

Ta	x	$E_{a1}$ (eV)	Range (K)	$E_{a2}$ (eV)	Range (K)	$\sigma_{RT} (\Omega^{-1} \cdot cm^{-1}) \times 10^{-4}$
RT	0.1	0.148	283-363	0.685	363-473	0.126
	0.3	0.125	283-363	0.645	363-473	0.131
	0.5	0.124	283-363	0.635	363-473	0.505
	0.7	0.034	283-363	0.598	363-473	0.785
	0.9	0.026	283-363	0.58	363-473	2.227

**Table 4. Hall parameters for  $Pb(Zr_x, Ti_{1-x})O_3$  films with different x-concentration at RT**

Ta	x	$R_H \times 10^7$	$\mu (cm^2/V.s) \times 10^6$	$\sigma (\Omega \cdot cm)^{-1} \times 10^{-4}$	$\rho (\Omega \cdot cm) \times 10^4$	$n (cm^{-3}) \times 10^{11}$	type
RT	0.1	6.27	7.92	0.126	7.91	0.99	p
	0.3	4.05	5.29	0.131	7.65	1.54	p
	0.5	8.82	4.45	0.505	1.98	7.08	p
	0.7	0.413	3.24	0.785	1.27	15.1	p
	0.9	0.143	3.19	2.23	0.45	43.6	p

## 4. Conclusions

The structural, optical and electrical properties of grown  $\text{Pb}(\text{Zr}_x\text{Ti}_{1-x})\text{O}_3$  with different concentration deposited on glass are investigated. The samples are scanned at room temperature, they were very sensitive to the change in Zr concentration. The phase were perovskite with a polycrystalline structure. Optical energy gap decreases from (3.41 to 3.21) eV with increasing Zr concentration from (0.1 to 0.9). There are two transport mechanisms of the charge carriers in the range of temperatures (283–473) K. It was found that the activation energy values ( $E_{a1}$ ,  $E_{a2}$ ) decreased with the increase of Zr concentration but the d.c. conductivity ( $\sigma$ ) increased with the increasing of concentration of Zr. Hall measurements showed that all the films were p-type. carriers concentration were directly proportional with Zr concentration but mobility were inversely proportional with Zr concentration.

## References

- [1] F. Švegl, B. Orel, & V. Kaučič, "Electrochromic properties of lithiated Co-oxide ( $\text{Li}_x\text{CoO}_2$ ) and Ni-oxide ( $\text{Li}_x\text{NiO}_2$ ) thin films prepared by the sol-gel route," *Sol. Energy*, vol. 68, no. 6, pp. 523-540, (2000).
- [2] M. Morozov, "Softening and Hardening Transitions in Ferroelectric  $\text{Pb}(\text{Zr,Ti})\text{O}_3$  Ceramics," vol. 3368, (2005).
- [3] M. Prabu, "Studies of pure and doped Lead Zirconate Titanate ceramics and PLD PZT thin films". PH.D Thesis, B.S. Abdur Rahman University, (2013).
- [4] J. Ma, J. Hu, Z. Li, & C.-W. Nan, "Recent progress in multiferroic magnetoelectric composites," *Adv. Mater.* 23, p-1062, (2011).
- [5] C. Jégou, L. Michalas, T. Maroutian, G. Agnus, M. Koutsourelis, G. Papaioannou, L. Largeau, D. Troadec, A. Leuliet, P. Aubert & Ph. Lecoeur, "Temperature dependence of the conduction mechanisms through a  $\text{Pb}(\text{Zr,Ti})\text{O}_3$  thin film," *Thin Solid Films* 563, p-32, (2014).
- [6] G.H. Haertling, "Ferroelectric ceramics: History and technology," *J Am Ceram Soc.* 82: p 797-818, (1999).
- [7] K. Srinivas, "Influence of nanoparticles in PZT ferroelectric material properties and their applications to memory devices," *Am. J. of Nano science and Nanotechnology*; 2(3) p-56-62, (2014).
- [8] K. Tahmasebi, & A. Barzegar, "Multiferroic Thin Film Composite of  $\text{Pb}(\text{Zr}_{0.52}\text{Ti}_{0.48})\text{O}_3$  and Co-50%Fe Alloy," *Transaction F: Nanotechnology*, Vol. 17,p- 108,112,(2010).
- [9] C. T. Q. Nguyen, M. D. Nguyen, M. Dekkers, E. Houwman, H. N. Vu, & G. Rijnders, "Process dependence of the piezoelectric response of membrane actuators based on  $\text{Pb}(\text{Zr}_{0.45}\text{Ti}_{0.55})\text{O}_3$  thin films," *Thin Solid Films*, 556, p-509–514, (2014).
- [10] W. Zhu, W. Ren, H. Xin, P. Shi & X. Wu, "Enhanced ferroelectric properties of highly (100) oriented  $\text{Pb}(\text{Zr}_{0.52}\text{Ti}_{0.48})\text{O}_3$  thick films prepared by chemical solution deposition," *J. of adv. Dielectrics*, Vol. 3, No. 2, 1350011, (2013).
- [11] M. D. Nguyen, H. N. Vu, D. H. A Blank & G. Rijnders, "Epitaxial  $\text{Pb}(\text{Zr, Ti})\text{O}_3$  thin films for a MEMS application," *Adv. Nat. Sci.: Nano sci. Nano technol.* 2, 015005, (2011).
- [12] C. Kittel, "Introduction to Solid State Physics," Eight Edit. John Wiley and Sons., (2005).
- [13] L.V.Azaroff, "Elements of X- Ray Crystallography," McGraw-Hill, Inc., (1968).
- [14] L. U. Jian, J. C. Hu, W. H. Uang, & Z. P. Ing, "Preparation of Thick  $\text{Pb}(\text{Zr, Ti})\text{O}_3$  (PZT) Film by Electrostatic Spray Deposition (ESD) for Application in Micro-System Technology," *Appl. Phys.*, vol. 41, no. 6, pp. 4317-4320, (2002).
- [15] S. Kim, J. Yang, C. Y. Koo, J. Yeom, D. Lee, & J. Ha, "Electromechanical Properties of  $\text{Pb}(\text{Zr, Ti})\text{O}_3$  Films for MEMS Applications," vol. 42, no. April, pp. 1101-1104, (2003).
- [16] P. S. Kireev, "Semiconductors physics," 2nd edition. translated from the Russian by M. Samokhvalov, Mir publishers Moscow, (1978).
- [17] A. Islam, M. Islam, M. Choudlury & M. Hassan, "Recent Velopment in Condenced Matter Physics and Nuclear Science," no. Rajshahi University, Bangladesh, (1998).
- [18] T. Kamakshi & P. S. V. SubbaRao, "Softening transitions in ferroelectric  $\text{Pb}(\text{Zr, Ti})\text{O}_3$  ceramics doped with neodymium oxide and lanthanum oxide," *J. Appl. Phys.*, vol. 6, p. 50-55, (2014).
- [19] K. Wafaa, D. Sariya & R. Sura, "Structure and Morphological Properties of Cadmium Oxide Nanostructure Prepared By Oblique Angle Deposition Method," *ICNAMA*, (2015).
- [20] A. Khorsand & W. Majid, "Effect of solvent on structure and optical properties of PZT nanoparticles prepared by solgel method, in infrared region," *Ceram. Int.*, vol. 37, pp. 753-758, (2011).
- [21] J. Puustinen, "Pase structure and surfase morphology effects on the optical properties of nanocrystalline PZT thin films," *Universty of Oulu*, (2014).
- [22] L. Holland & G. Siddall "the properties of some reactively sputter 4ed metal oxide films," *Vacuum*, vol. 3.4, pp. 375-391, (1953).
- [23] M. Moret, M. Devillers & K. Worhoff, "Optical properties of  $\text{PbTiO}_3$ ,  $\text{Pb}(\text{Zr}_x\text{Ti}_{1-x})\text{O}_3$ , and  $\text{PbZrO}_3$  films deposited by metalorganic chemical vapor on  $\text{SrTiO}_3$ ," *J. Appl. Phys.*, vol. 92, no. 1, pp. 468-474, (2002).